electronics

MDPI

Article

Electrothermal Aging Model of Li-Ion Batteries for Vehicle-to-Grid Services Evaluation

Maria Stefania Carmeli [1], Nicola Toscani [2] and Marco Mauri [2,*]

[1] DEIB Politecnico di Milano, 20133 Milano, Italy; stefania.carmelil@polimi.it
[2] DMECC Politecnico di Milano, 20156 Milano, Italy; nicola.toscani@polimi.it
* Correspondence: marco.mauri@polimi.it; Tel.: +39-022-3998-377

Abstract: The growing interest in Electrical Vehicles (EVs) opens new possibilities in the use of Li-ion batteries in order to provide ancillary grid services while they are plugged to recharging stations. Indeed, Vehicle-to-Grid (V2G), Vehicle-to-Building (V2B), Vehicle-to-Home (V2H) as well as Vehicle-to-Vehicle (V2V) services can be carried out depending on the particular installation and on the connection to the distribution grid of the considered recharging station. Even if these are interesting and challenging opportunities, the additional charging/discharging cycles necessary to provide these services could decrease the expected life of EV batteries. For this reason, it is of paramount importance to study and develop reliable models of the batteries, which take the aging phenomena affecting the reliability of the Li-ion cells into account to evaluate the best charging/discharging strategy and the economic revenues. To this aim, this paper focuses on a battery pack made up with Li-ion nickel–manganese–cobalt (NMC) cells and proposes a semiempirical Electrothermal Aging Model, which accounts for both calendar and cycle aging. This modeling phase is supported by several experimental data recorded for many charge and discharge cycles at different C-rates and for several temperatures. Thus, it is possible to analyze and compare scenarios considering V2G services or not. Results show that the considered battery is subjected to a life reduction of about 2 years, which is a consequence of the increased Ah charge throughput, which moves from 120,000 Ah over 10 years (scenario without V2G services) to almost 230,000 Ah over 8 years (scenario with V2G services).

Keywords: electrical vehicles; vehicle to grid; aging model; Li-ion NMC batteries

Citation: Carmeli, M.S.; Toscani, N.; Mauri, M. Electrothermal Aging Model of Li-Ion Batteries for Vehicle-to-Grid Services Evaluation. *Electronics* **2022**, *11*, 1042. https://doi.org/10.3390/electronics11071042

Academic Editor: Pablo García Triviño

Received: 4 March 2022
Accepted: 24 March 2022
Published: 26 March 2022

1. Introduction

Nowadays, the transportation industry and the automotive one in particular is going through a transition from Internal Combustion Engine (ICE) vehicles to Electrical Vehicles (EVs), with the main goal of meeting EU targets to reduce the CO_2 emissions from the road transport sector. In this scenario, battery technology is the heart of this transition as main parts in terms of performances, affordability and reliability of hybrid and full electric vehicles [1–3]. In this scenario, Lithium-ion (Li-ion) batteries play a key role due to their high gravimetric energy density (Wh/kg), volumetric energy density (Wh/L) and power density (W/kg) [4].

However, the growth of e-mobility introduces some new problems in the electric grid that are important to analyze. Indeed, the average consumption for a Battery Electric Vehicle (BEV) is around 0.18 kWh/km and the average annual distance is around 11,500 km (EU average). Thus, each BEV is expected to need almost 2070 kWh in one year [5]. According to these data, the impact of EV charging on the daily load curve could be a serious problem because, even if the installed capacity could supply this new demand, the distribution system components (such as transformers and lines) would be overloaded, with consequent congestions and reduction of their lifetime [6].

For this reason, electric vehicle integration in the grid has to be smart and controlled. Considering that private vehicles spend 95% of their lifetime being parked [7], if they were

plugged EVs they could allow the bidirectional flow of power, enabling the Vehicle-to-Everything (V2X) service and the interaction of the vehicle with other systems: Vehicle-to-Building (V2B) and Vehicle-to-Home (V2H) to increase the self-consumption coming from distributed generation (DG); Vehicle-to-Vehicle (V2V) to allow mutual support between vehicles; Vehicle-to-Grid (V2G) to turn the electric vehicle from a potential threat to a distributed battery energy storage system able to provide all or some grid services.

However, the full implementation of V2G has still some important issues to be solved: a widespread charging infrastructure to allow vehicles connection; favorable policies and a renewed electricity market that allows adequate revenues; an EV equipped with advanced power electronics devices and with a battery pack that does not suffer too much from the additional cycling; an aggregator to integrate and coordinate all these distributed resources through data communication; and an intelligent energy management, as a unique actor participating on the electricity market.

Among all these aspects, understanding the aging phenomena of the battery is of particular importance to describe its performances and reliability in terms of lifetime [8,9], allowing to perform the previous services. Each battery, whether it is used or not, suffers from a continuous reduction of its useful capacity (the amount of charge that can be extracted from the battery, measured in Ah) and an increase in the internal series resistance, which leads to a decrease in the available output power. A battery reaches the end of life (EOL) when the capacity loss, measured with respect to the nominal one, equals either 20% [10–12] or 30% [13].

Therefore, the modeling of the aging phenomena is a key issue. First, an aging model could be used to quantify the increased capacity fade due to the additional cycling of the batteries subjected to V2G and compare them to the unavoidable calendar aging loss of a parked EV. Based on this model, a battery-management system could be implemented to avoid highly detrimental operating conditions for the vehicle, working on middle state of charge (SOC), depth of discharge (DOD) and C-rate stress factors. At a higher level, the knowledge of the aging status for more EVs could be used by an aggregator to provide V2G services in an optimized way considering all the different EVs parked. Finally, the battery initial cost and its aging are fundamental to evaluate the proper revenue for the driver and the aggregator that provides ancillary services [14].

This paper presents an analysis of a Li-ion nickel–manganese–cobalt (NMC) batteries considering an electro-thermal model in order to analyze different scenarios for the Vehicle-to-Grid (V2G) services in terms of battery degradation. To this aim, an overview of the aging models that were developed has been presented and, after that, an aging model is developed starting from experimental data to analyze a V2G scenario. The paper is organized as follows: Section 2 describes the Li-ion batteries' aging phenomena; Section 3 provides a literature review of the models used to describe these phenomena; Section 4 presents the electrothermal model used in this paper to describe a Li-ion NMC battery; Sections 5 and 6 present the calendar aging model and the cycle aging model respectively; in Section 7 different V2G scenario are presented and compared in terms of battery degradation; and, finally, Section 8 draws the conclusions of the paper.

2. Aging Phenomena

Aging occurs whenever the performance of a battery deteriorates over time, due to a continuous reduction of its useful capacity and an increase of the internal series resistance, which leads to a decrease in the available output power [8,15]. The chemical components stored in each cell at the beginning of its life are at a high energy state, which one would like to exploit to convert chemical energy into electrical energy and vice versa according to Equation (1).

$$Li_xC_y + Li_{1-x}MO_2 \rightleftarrows yC + LiMO_2 \quad (1)$$

Unfortunately, the anode, cathode, separator and electrolyte interact between each other during cycling and storage in such a complex way that many side reactions occur in the cell, depending on factors such as SOC, temperature and C-rate [16]. These side

reactions evolve toward a more stable, lower energy state, in an irreversible way that leads to electrolyte degradation, loss of active material at the anode/cathode or loss of cyclable lithium, where all contribute to capacity fade and resistance increase.

2.1. Aging on the Negative Electrode-Electrolyte Interface

The critical area where the side reactions take place is the interface between electrolyte and electrodes. Particularly, the main aging process happens at the carbon electrode–electrolyte interface, with the development of the so-called Solid Electrolyte Interphase (SEI) [16–18]. The typical graphite anode works outside the electrolyte stability window, so, during the first cycles of a new cell, a reaction between intercalated Li+ and the electrolyte solution creates this SEI, forming a protective layer that prevents further degradation of the graphite anode and allows a stable operation, as SEI is permeable to Li+. However, the SEI is porous and some electrolyte can diffuse and reach the anode surface. Moreover, charging and discharging the cell with the intercalation/deintercalation of Li+ causes up to 10% variation in the volume of the graphite anode, cracking the SEI. Both phenomena lead to a continuous thickening of the SEI layer, with an irreversible loss of cyclable lithium and electrolyte. Furthermore, as the SEI layer increases, so too does the cell resistance. The solvent particles may also interact with the electrode causing graphite exfoliation, which results in loss of active material and gas formation [16]. It is important to state that lithium titanium oxide (LTO) cells do not face any SEI formation, with batteries that have shown lower capacity fade and longer lifetime compared to the graphite-based one [17]. The price to pay is a lower energy density for LTO batteries, due to the lower voltage for the single cell. In addition to surface film formation and active material degradation, another aging mechanism occurring at the anode surface is lithium plating. When the intercalation reaction becomes too slow and the potential too low, lithium ions start to deposit onto the anodic graphite forming a metallic structure. This consumes cyclable lithium and it is also a safety risk, as metallic lithium can form dendrites and lead to hazardous short-circuits between the electrodes [13].

2.2. Aging on the Positive Electrode-Electrolyte Interface

The aging phenomena occurring at the cathode can be classified into surface film formation and active material degradation. In the first case, the coating may arise from the side reactions between the electrolyte and the cathode. Instead, during the charge and discharge of the cell, cathodic materials may face changes in the lattice structure with the dissolution of the transition metal ions [13]. This results in loss of active material, with ions that might also migrate to the anode SEI surface and increase its thickness. Lithium manganese oxide (LMO) cells are the most sensible to degradation due to crystal deformation and dissolution of manganese Mn2+ ions inside the electrolyte, followed by lithium iron phosphate (LFP) and NMC. However, all these phenomena have lower impact on aging than those occurring at the anode interface, as the cathode does not operate at high voltage (around 4.5 V) where film formation and degradation are enhanced [8].

2.3. Calendar and Cycle Aging

Although the aging phenomena described before occur whether the battery is used or not, it is typical to divide battery degradation into calendar aging and cycle aging.

Calendar aging refers to the storage conditions, i.e., when the battery is not operating. In this condition, the capacity fade can be divided into a reversible capacity loss (RCL), also called self-discharge, that can be recovered recharging the battery after the storage, and an irreversible capacity loss (ICL), which is permanently lost [15]. The main parameter affecting calendar aging is the storage temperature T: the higher it is, the easier side reactions will occur. SOC is another important factor, as cell stored at high SOC show increased capacity fade. This could be explained by the higher potential disequilibrium at the electrode–electrolyte interface due to higher SOC [18–21].

Cycle aging is associated with battery operation, i.e., with the charge and discharge cycles. While aging on storage is due to side reactions resulting from the thermodynamic instability of materials in presence, cycling adds kinetically induced effects, such as volume variations, or concentration gradients [15]. Therefore, cycle aging will also depend on other factors such as middle SOC, SOC variation, that is, DOD, and the C-rate.

3. Aging Models Literature Review

The cross-interaction of temperature, SOC and C-rate on the battery-aging mechanisms makes it challenging to create suitable models for lifetime prediction. In the current literature, three main categories can be identified, namely electrochemical–mechanical models, equivalent circuit models and empirical models.

3.1. Electrochemical-Mechanical Models

The goal of electrochemical–mechanical models is to describe the aging phenomena using physical equations. These models focus on SEI formation and on its evolution at graphite anodic surface, because this is the dominant phenomena that leads to a capacity reduction.

Purewal et al., in [22], tested NMC batteries developing a model for both chemical and mechanical degradation in good agreement with the capacity loss predictions of the companion paper [13]. They focused on modelling fatigue crack growth at the graphite particle surface from repeated diffusion-induced stresses (DIS) during cycling and growth of the SEI film thickness under diffusion-limited processes. Another study [23], also takes into account Li+ diffusion according to Fick's law, adding the description of the intercalation/deintercalation current with Butler–Volmer equation and focusing on thermal aspects, building a unique thermal–electrochemical model. They pointed out how SEI growth is faster during charge than discharge and that temperature rise in Li-ion batteries accelerates the SEI layer growth [23]. In [24], a different point of view is highlighted by studying the effect of the potential drop across SEI and consequent capacity fading. Based on Eyring equation, ref. [11] tried to use a simple expression to describe the kinetics of the electrochemical side reactions occurring during battery aging. The result is a model able to compute the number of cycles according to the specific temperature, DOD and C-rate operation, until reaching the EOL, set at the 80% of available nominal capacity. The model [11] performs quite well as a cross-over one, linking internal processes to external phenomena, but it has no calendar-aging behavior included. In [18], the effects of an extended cycling in mild conditions are highlighted, due to the formation of lithium plating, predicted by a physics-based model. It takes into account how SEI formation and growth produces a linear increase in the capacity loss in the first stage. In a second stage, when SEI growth has reduced anode porosity, the lithium-plating reaction becomes the predominant one, in a positive feedback loop that makes the aging process during cycling strongly nonlinear [18].

On one hand, these models, which require a detailed understanding of the underlying chemical processes, give good results in the description and prediction of microscale phenomena, perhaps affecting different batteries with similar structures, such as with a graphite anode. On the other hand, the link between all these different effects and their global description in a macroscale way are still a great challenge for an overall modelling of battery aging.

3.2. Equivalent Circuit Models

Equivalent circuit models are based on the Electrochemical Impedance Spectroscopy (EIS) technique, which is recognized as a nondestructive characterization technique to understand the electrochemical processes in a cell and how they change over time [25]. EIS can be performed applying an ac sinusoidal current or voltage over a wide range of frequencies (from mHz to kHz and more), measuring the voltage or current response respectively, and evaluating the equivalent cell impedance. Equivalent circuits with a

single voltage sources in series with a variable number of RLC series/parallel branches are usually proposed [25–28]. The evolution of these RLC parameters are usually obtained with accelerated tests where cells are subjected to different temperature, SOC, DOD and C-rates. Equivalent circuit models come from a macroscale approach describing the overall effects of multiple factors impacting the battery aging, which can refer to the single battery technology. Furthermore, the use of an equivalent circuit could help in more general and effective description of multiple aspects related to the battery, such as its management system. One drawback of this approach is that it requires a large amount of experimental data, leading to time- and cost-consuming processes for the model evaluation.

3.3. Empirical Models

The last and widest class is the one of empirical models. Empirical models focus on the battery as a black box, testing the battery at different combinations of temperatures T and SOCs for calendar aging tests. For cycle aging tests, different current profiles are used, with different charging/discharging C-rates. The final evaluation is based on the capacity-fade measurement, which is periodically characterized depending on specific charging/discharging operations defined time-by-time by the authors, and on the measurement of the internal resistance, according to the pulse-resistance test [25,29].

Instead of focusing on a specific circuit, the empirical models pull out experimental trends for the description of capacity fade and internal resistance as function of time, for calendar aging, or function of the number of cycles, for cycle aging.

For example, ref. [12] focuses on the cycle aging of LFP 2.3 Ah batteries by evaluating the influence of temperature (−18, 0, 25, 40 °C), DOD (20%, 40%, 60%, 80%, 100%) and C-rate once at a time, so when the other two parameters are set at their nominal values. A prediction model is developed according to the exponential trends obtained for the number of remaining cycles as function of T, DOD and C-rates, with a maximum error between experiments and simulations of 5.4%. However, there is no focus on calendar aging aspects in [12], but they are pointed out in [30] by Grolleau et al. In this paper, the model is built based on the Arrhenius relationship for capacity fade during calendar aging, which is commonly used in the literature.

Wang et al. also focused on LFP 2.2Ah batteries in [31], using a different approach, based on a test matrix made up of six temperatures (−30, 0, 15, 25, 45, 60 °C) five DOD (90%, 80%, 50%, 20%, 10%) and four constant C-rates (C/2, 2 C, 6 C and 10 C) and developed a predicting model. To sum up, empirical models represent a widely exploited solution to provide a powerful prediction of aging evolution under different stress factors, without a detailed comprehension of physical–chemical models, making them suitable as blocks inside a global system model such as a vehicle model [32]. The drawback, also in this case is the required wide data set, although an optimal design of experiments could be developed to reduce time and cost consumption [32].

4. Electrical and Thermal Model

Li-ion batteries are the most used in EVs due to their high energy and power density, high efficiency and long cycle lifetime. Li-Ion batteries identify a large family of batteries that work with Li+ ion flow, having different material at the anode, cathode and electrolyte for the single cell [9]. For EV applications, the automotive industry mainly focuses on the nickel–cobalt–aluminum (NCA, $LiNiCoAlO_2$) and nickel-manganese-cobalt (NMC, LiNixMnyCo1-x-yO_2) technology (Table 1) [2]. Both technologies have a cell voltage greater than 4 V when fully charged, and they require an efficient active management system to ensure high safety levels.

Table 1. Li-ion chemistry of some EV batteries (2017 data).

Model	Chemistry	Cell Manufacturer
Tesla Model S, X	NCA	Panasonic
BWM i3	NMC	Samsung
Nissan Leaf	NMC	AESC
Renault Zoe	NMC	LGChem
Volkswagen e-Golf	NMC	Samsung

So, focusing on NMC type, in Li-ion cell modeling, it is of paramount importance to predict and analyze its behavior in different operating conditions. Three main types of models can be found in the literature to describe a Li-ion NMC battery: electrochemical, empirical and electrical models [14].

Electrochemical models resort to chemical kinetics and thermodynamics, involving coupled partial differential equations and a deep knowledge of electrochemistry. They are able to predict many phenomena occurring inside a cell through complex modeling. Empirical models consider the battery as a black box, connecting the external variables of interest with few equations obtained from the analytical fitting of large sets of experimental data. Thus, they do not focus on the underlying chemical processes. Electrical models try to represent the cell with an electric circuit that shows the same current-voltage characteristic at the external terminals. The cell layers are modeled by electric components such as resistors, capacitors and voltage sources, where the complexity of the model can vary in a wide range depending on the number of adopted parameters.

To sum up, electrochemical models are complex and quite inefficient from the computational point of view at a system level, where the cell is a part of a structure, such as a battery, that in turn belongs to a system, e.g., an electric vehicle. Empirical modeling is easy to use, but each model is specific for one application. This requires large sets of experimental data and it can be affected by large errors with reduced fidelity of the simulations. On the other hand, electric circuit models (ECMs) are easier to manage, computationally more efficient than electrochemical ones, and with a good accuracy in predicting the battery performances under different conditions. In this paper, an electrical model is used to predict the cell battery behavior [33].

The Li-ion cell is just the basic unit of a bigger system which is the battery pack (Figure 1). In EVs, the cells are connected in series and parallel to reach certain current and voltage levels. Furthermore, to safely mange the cells, they are installed in modules and packs. In modules, cells are gathered into a frame to protect them from external shocks and more modules are connected to create a battery pack. At module level, it is necessary to control and manage temperature with a Thermal Management System (TMS) and voltage with a Battery Management System (BMS).

The BMS is necessary to achieve the cell balancing at module level, whereas TMS is needed because cells are subjected to different temperatures depending on their position inside the battery pack. In this paper, BMS and TMS are considered ideal, assuming a perfect cell balancing and a uniform battery temperature due to an efficient cooling system. In order to validate this hypothesis, some tests have been performed using 15 cells connected in a single series branch and 16 cells connected in two parallel branches of 8 series cells. The module is discharged with a constant current of 31 A for 600 s. Preliminary tests show that single cell parameters vary uniformly by around 2% of their nominal values. At the end of the test, the final SOC unbalance is around 1% between different cells for the series-connected module and 1.5% for the parallel-connected module (Figure 2).

Figure 1. Li-ion cylindrical cells arranged in modules to form the EV pack.

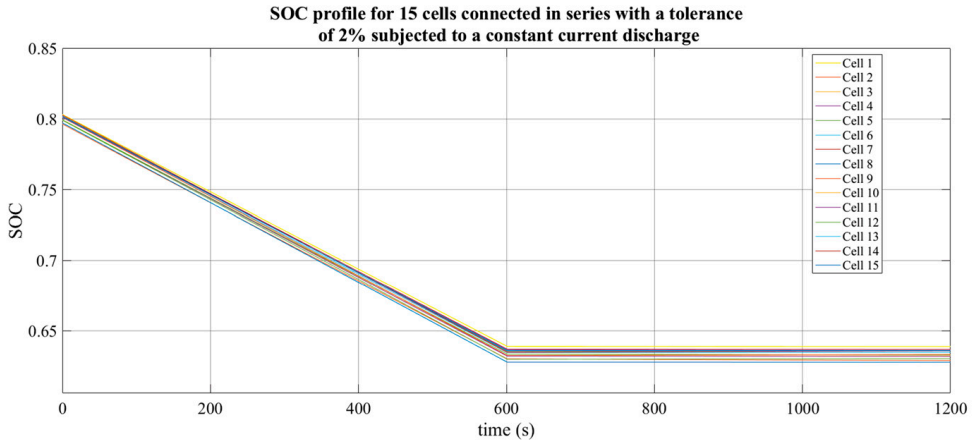

(**a**)

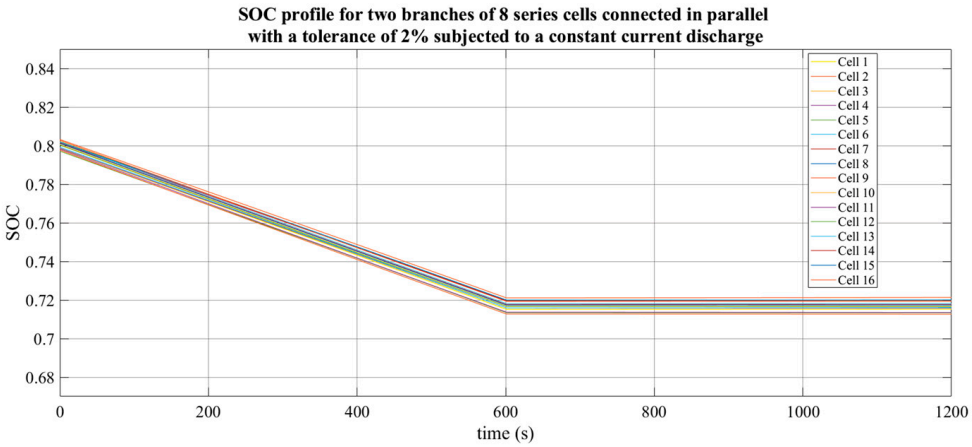

(**b**)

Figure 2. SOC unbalance for a constant current discharge: (**a**) 15 cells series connected (**b**) 8 series cells parallel connected.

The 15 series cells module is also used to validate the TMS approximation. During the 1200 s discharge transient, the cell temperatures is monitored and the maximum observed variation between two cells is less than 1 °C with active TMS control. The maximum

difference has been observed between the eighth cell (central cell in the module) and the first cell.

A battery pack consists of a series connection of 100 NMC cells in order to reach a nominal voltage level of 370 V, which has been chosen to develop the electrothermal model. Three series branches are parallel connected to reach a capacity of 93 Ah and a nominal energy of 34.4 kWh according to the technical specifications of actual EVs (Table 2).

Table 2. Energy and voltage ratings of Li-ion batteries installed on selected EVs (2017 data).

Model	Energy [kWh]	Battery Voltage [V]
Tesla Model S, X	40, 60, 85	300
BWM i3	33.2	353
Nissan Leaf	24, 40	350
Renault Zoe	22, 41	400
Volkswagen e-Golf	35.8	323

4.1. Thermal Model

Assuming a uniform battery temperature T, it is possible to model the thermal behavior using a first-order thermal circuit (Figure 3), where C_{th} is the cell heat capacity, R_{th} is the convective thermal resistance and P_{losses} the internal battery power losses. A first-order model is chosen due to the model simplicity and based on the hypothesis of an ideal TMS control. The two parameters are calculated as indicated in Equation (2) where m is the cell mass, c_t the specific heat capacity, h the heat transfer coefficient and A the convective exchange surface area. The heat transfer coefficient and the specific heat capacity are estimated using experimental data. Considering the entire battery pack, it is possible to assume the same network adapting the mass to the entire battery and the exchange area according to the cell position. In this paper, it has been considered that the 300 cells are arranged in 15 rows of 20 cells each. The heat transfer coefficient changes based on the adopted cooling fluid (h = 20–250 for forced air convection, h = 1600–2600 for forced glycol convection). T can be found solving the network shown in Figure 3.

$$C_{th} = c_t \cdot m, \; R_{th} = \frac{1}{h}A \tag{2}$$

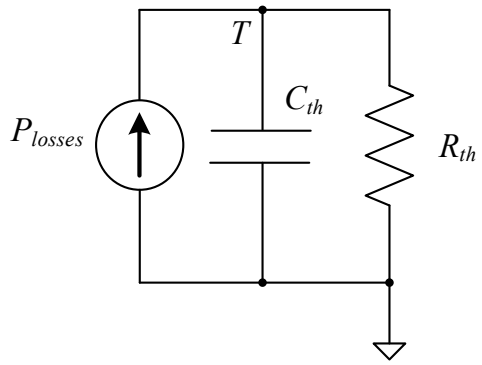

Figure 3. Cell thermal model.

4.2. Electrical Model

The electrical model used in this paper is shown in Figure 4. A single RC branch model is used where each component is written as a function of *SOC* and of the temperature T [34]. The temperature has been calculated using the previous thermal model.

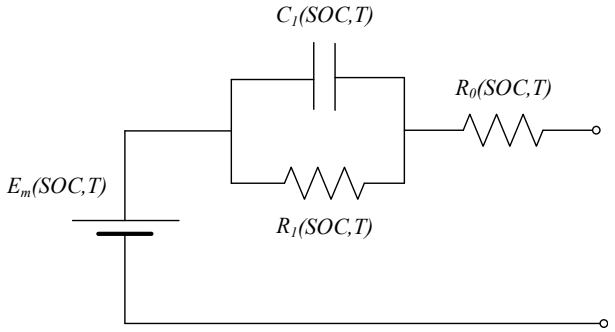

Figure 4. Cell electric model.

The *SOC* is computed using Equation (3), where Q_e is the charge extracted from the cell and C_Q is the cell capacity. Q_e is calculated based on the discharge current I as shown in Equation (4).

$$SOC = 1 - \frac{Q_e}{C_Q} \tag{3}$$

$$Q_e(t) = \int_{t_0}^{t} I(\tau)d\tau + Q_e(t_0) \tag{4}$$

when computing *SOC*, it is important to point out that in general cell capacity C_Q is not a constant value. It depends on many factors, such as: the storage time, because of self-discharge; the operating temperature and the discharge current, which are related to each other, because the higher the discharge current the more the cell heats up; and the aging effects related to capacity fade on a long time scale. Peukert's law Equation (5) is typically used when computing cell capacity where C_Q is the cell capacity, I_n is the nominal cell current and t is the time. Due to the factor k being greater than 1, a discharge with a C-rate of, e.g., 2C (twice the nominal current to discharge the cell in 1 h) affects the cell capacity, which will be lower and cause the cell to be discharged in less than half an hour.

$$C_Q = I_n t^k \tag{5}$$

Nevertheless, some useful hypotheses can be created for the Li-ion cell. First, C_Q has very small changes in the temperature range in which the cell typically operates. Second, Li-ion cells do not suffer from self-discharge in practice. In addition, coefficient k in Equation (4) is slightly greater than 1 (1.03–1.05), so, if the cell is discharged from 0.25 C to 2 C (twice the nominal current to discharge the cell in 1 h), C_Q changes its value of only few percent compared to the nominal one. For these reasons, C_Q can be considered constant on a short time scale. Long time-scale effects could be considered only in an aging model.

The analyzed Li-ion cell is a 31 Ah NMC pouch cell, whose specifications are reported in Table 3. The cell was iteratively tested with the pulse discharge characterization tests, subjected to partial constant current discharges followed by a rest phase to recover the Open Circuit Voltage (OCV), as in Figure 5.

Table 3. Technical specifications of the Li-ion cell considered for this study.

Characteristic	Value
Nominal Capacity	31 Ah
Nominal Voltage	3.7 V
Voltage range	3.4–4.2 V
Maximum continuous current	155 A
Maximum peak current	310 A
Operating temperatures	Charge: 0 °C–40 °C Discharge: −20 °C–60 °C
Thickness	8.4 mm
Width	215 mm
Length	220 mm
Weight	1 kg

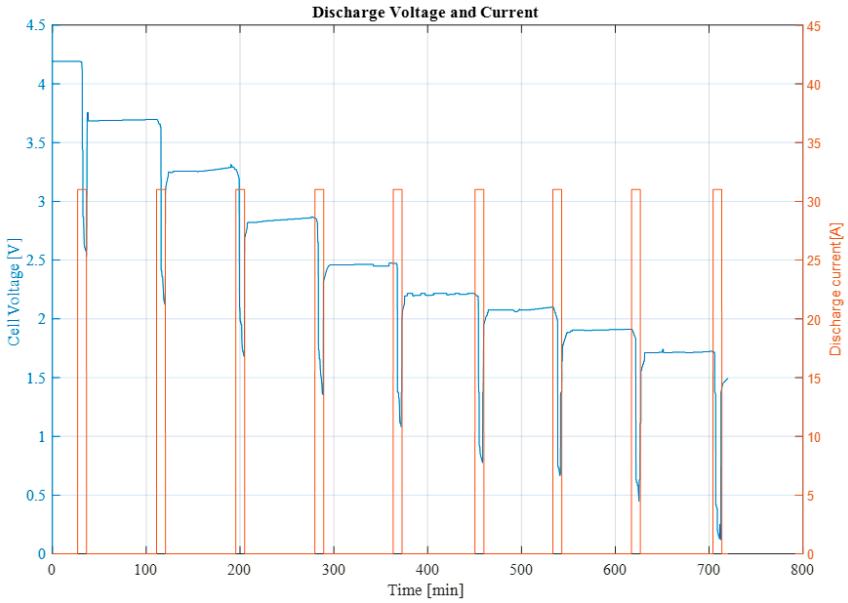

Figure 5. Experimental discharge curves at 20 °C.

To simplify the electrical parameters calculation during the simulation phase, some look-up tables are used. In particular, three different temperatures (5, 20 and 40 °C) and seven SOC breakpoints (0, 10, 25, 50, 75, 90, 100%) are chosen.

Regarding the estimation procedure of the electrical parameters, each temperature is considered independently and simulated data is fitted over the experimental one using the nonlinear least squares algorithm, allowing us to obtain the results shown in Figure 6.

The electromotive force is mainly influenced by SOC and, practically, it does not change with temperature. Both resistances show lower values for middle SOC and they increase when temperatures decrease, which hinders the cell reaction. The capacitance, that accounts for the cell transient response, increases with temperature and it also shows two peaks around 20% and 80% SOC, which might be due to the internal phase transitions of the cell components.

Regarding the thermal parameters, a cell specific heat capacity of 810.53 J/kgK and a convective heat transfer coefficient between the cell and the environment (air natural convection) equal to 5 W/m^2K are obtained.

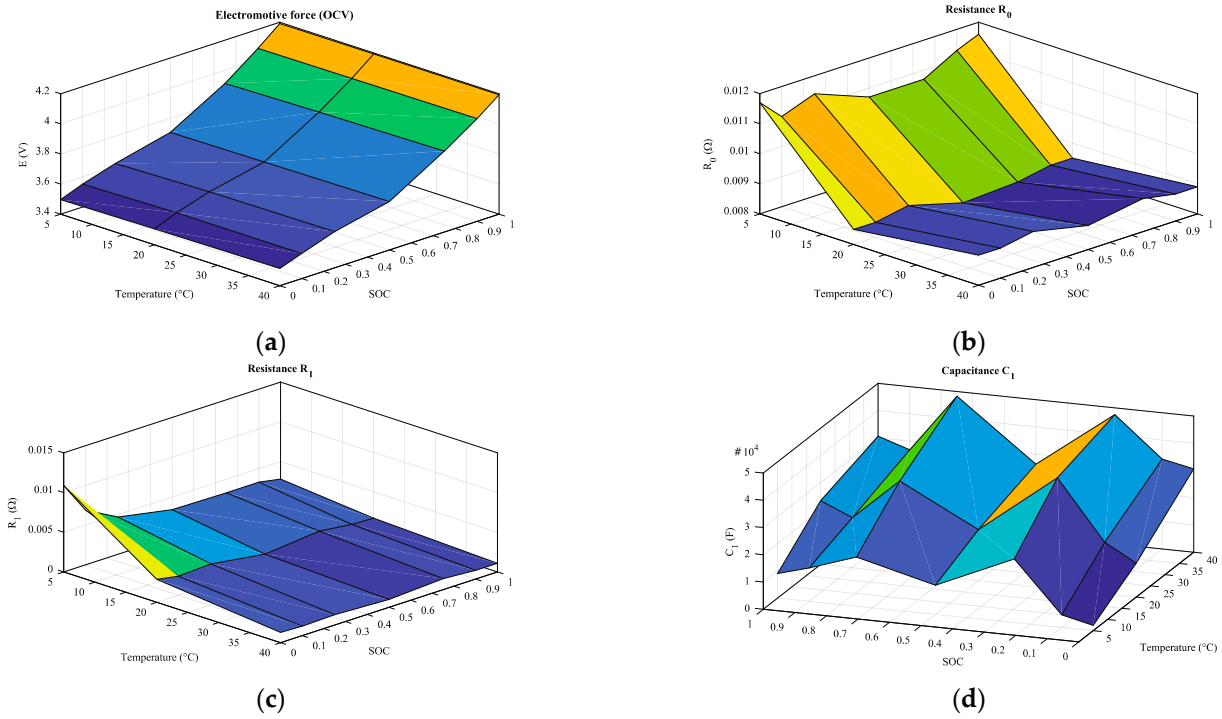

Figure 6. Experimental evidences for parameters E_m (**a**) R_o (**b**) R_1 (**c**) C_1 (**d**) as function of SOC and temperature.

5. Calendar Aging Model

Aging models aim at the description of the degradation of the cell until reaching the EOL. As described in Sections 2 and 3, they can be classified into three categories, namely, electrochemical models, empirical models and electrical models. Electrochemical models precisely describe the most important aging phenomena, such as SEI formation, lithium plating and mechanical degradation due to fatigue crack growth at the anode surface, according to the physical equations that govern them.

Electrical models rely on the same electric circuit described previously, but updating the parameters to keep track of the degradation through the years. This is done either with empirical equations that fit experimental data from accelerated aging tests or by using machine learning (ML) and artificial neural networks (ANN) to obtain the evolution of the parameters from periodic tests, such as the electrochemical impedance spectroscopy (EIS).

Empirical models also rely on extensive experimental campaigns, aiming at the estimation of the State of Health (SOH) to keep track of cell degradation. They consider the battery as a black box, which is tested for different combinations of temperatures and SOC for calendar aging tests and with different DOD and charging/discharging C-rates for cycle aging tests. Instead of focusing on a specific circuit, the empirical models estimate SOH by pulling out experimental trends for capacity fade and internal resistance as function of time, for calendar aging, or function of the number of cycles, for cycle aging.

To sum up, in this case electrochemical models are complex and difficult to manage at system level. Electrical and empirical models are commonly used, although they rely upon extensive experimental campaigns and have to be used for specific applications in order to reduce large errors in the prediction of SOH. From this point of view, ML and ANN represent the most promising solutions to adapt each model to its own cell, with its own chemistry, with a good accuracy in predicting the battery degradation under different conditions. In this work, semiempirical models have been developed to estimate the aging of the battery pack modeled in Section 4. The semiempirical models use experimental data to determine the variables of the chemical equations used to describe the reactions of interest at a macroscopic level. Among them, the Arrhenius Equation (6) is very often used

when describing the reaction rate k of SEI formation, which is the main aging phenomena, and its temperature dependence [15–18].

$$k = A \cdot e^{-\frac{E_A}{RT}} \tag{6}$$

where A is a pre-exponential factor related to the total number of collision that could lead to the reaction, which has the dimensions of s^{-1} for first-order reactions, while the exponential is related to the probability of happening for the reaction that depends on the temperature T in K, gas constant R equal to 8.314 J $mol^{-1}K^{-1}$ and the activation energy E_A in J mol^{-1} (the minimum amount of energy that must be provide to start the reaction). Taking the natural logarithm of Equation (7) and considering the dependence between ln(k) and the inverse of temperature, an equation of a straight line is obtained Equation (8). The corresponding plot, also called an Arrhenius plot, is the way to demonstrate that the reaction rate obeys the Arrhenius equation and to compute factors A and E_A from the gradient and the intercept.

$$\ln(k) = -\frac{E_A}{RT} + \ln(A) \tag{7}$$

This relationship has been used to develop both the calendar and cycle aging models taking into account the capacity-fade evolution from experimental data. Due to a lack of data, the resistance increase has been neglected from the aging models, but it is commonly known to be the less-strict aging process, with capacity fade leading the degradation of the battery to the EOL defined at 80% of residual nominal capacity [18–21].

To develop the calendar aging model, NMC Li-ion cell with a nominal capacity of 63 Ah have been tested at five different temperatures (10 °C, 25 °C, 33 °C, 40 °C, 55 °C) and eight different storage SOCs (10%, 20%, 35%, 50%, 65%, 80%, 90%, 100%) for 450 days, with periodic characterization aimed at measuring the residual capacity after 30, 90, 180, 270, 360 and 450 days. The capacity fade evolution as a function of T and SOC is shown in Figure 7. To model the evolution of capacity loss $Q_{loss\%}$ as a function of time t, measured in days, the Arrhenius equation could be rearranged as in Equation (9), where the pre-exponential factor A and the activation energy E_A are functions of the SOC. The exponential term depends on the absolute temperature T and the time evolution goes with a power law t^z. The z exponential factor can be obtained by computing the natural logarithm of $Q_{loss\%}$ Equation (9), obtaining Equation (10).

$$Q_{loss\%}(SOC, T, t) = A(SOC) \cdot e^{-\frac{E_A(SOC)}{RT}} t^z \tag{8}$$

$$\ln(Q_{loss}) = \ln(A \cdot t^z) - \frac{E_A}{R}\frac{1}{T} \tag{9}$$

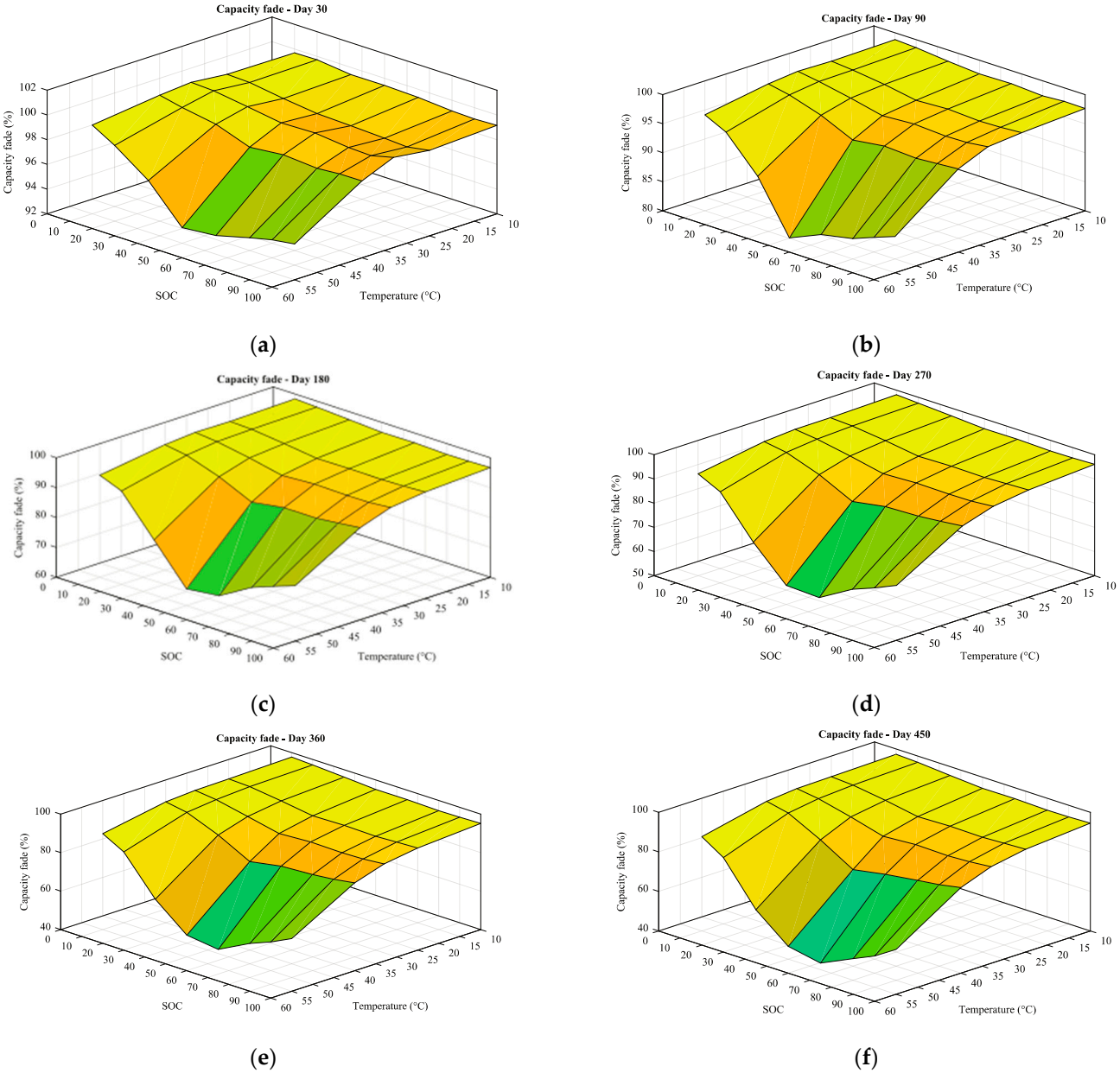

Figure 7. Experimental capacity-fade evolution from calendar aging test after 30 (**a**) 90 (**b**) 180 (**c**) 270 (**d**) 360 (**e**) 450 (**f**) days.

The Arrhenius plot is evaluated from Equation (9), after 270 days and for all storage SOCs, in order to verify that the capacity fade evolution obeys Equation (8). First, the linear relationship is verified at any SOC level, confirming the possibility of describing the capacity fade with Equation (8). After that, the activation energy E_A is obtained for all SOC as the slope of the fitted line multiplied by the gas constant R. The activation energy as a function of SOC is estimated with a third order polynomial function Equation (11) as highlighted in Figure 8 where SOC is expressed as a percentage (from 0 to 100).

$$E_A(SOC) = 0.05977 \cdot SOC^3 - 16.14 \cdot SOC^2 + 1232 \cdot SOC + 10710 \quad (10)$$

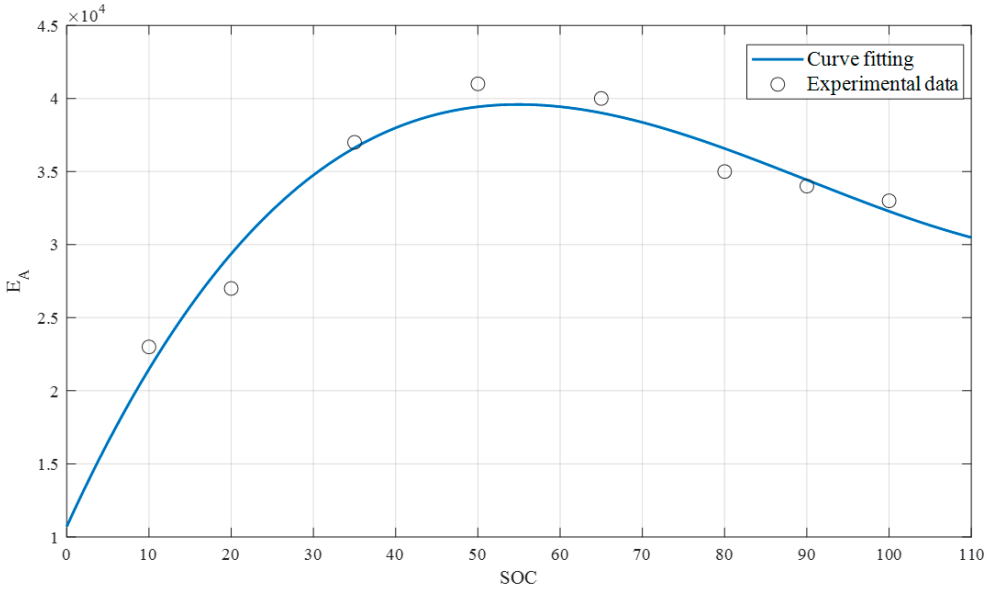

Figure 8. Curve fitting for the activation energy E_A as a function of SOC.

Once all values for E_A are obtained, Equation (9) can be rearranged further as reported in Equation (12) to obtain the logarithm of pre-exponential factor ln(A) as the intercept of the linear fitted curves for all SOC values. A third order polynomial function is used also in this case for ln(A) as in Figure 9. The pre-exponential coefficient A can be expressed as a function of SOC according to Equation (13).

$$\ln(Q_{loss}) + \frac{E_A}{RT} = \ln(A) + z\ln(t) \tag{11}$$

$$A(SOC) = e^{2.38\cdot10^{-5}SOC^3 - 0.006571\cdot SOC^2 + 0.5233\cdot SOC + 0.475} \tag{12}$$

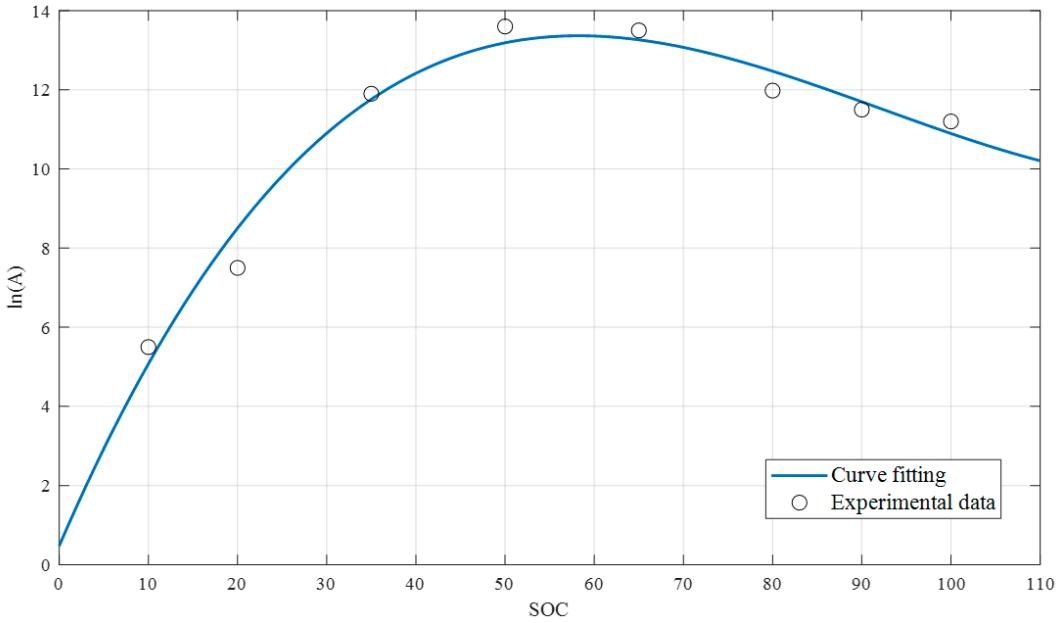

Figure 9. Curve fitting for the natural logarithm of coefficient a function of SOC.

Finally, the exponential coefficient z of the time is evaluated as the slope in Equation (12). Its value depends on both SOC and T ranging between 0.69 and 0.83,

so that a fitted surface z (SOC, *T*) is computed to match all possible operating conditions (Figure 10).

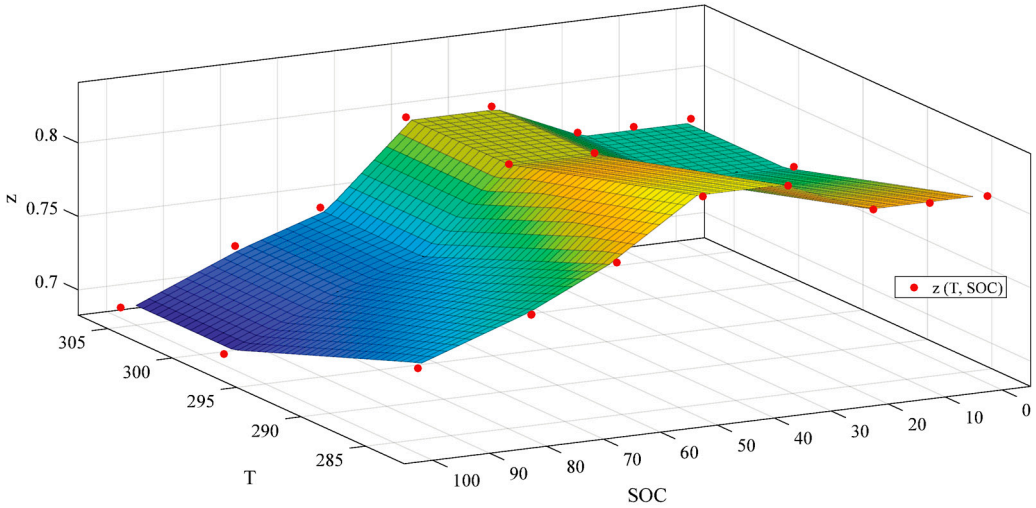

Figure 10. Surface fitting of the z coefficient as a function of temperature T and SOC.

The complete calendar model equation is reported in Equation (13). The developed model is able to follow the evolution of the capacity fade with errors within 1%. In Figure 11, some examples for different SOCs and temperature are shown.

$$Q_{loss,}\%(SOC,T,t) = e^{2.38\cdot10^{-5}\cdot SOC^3-0.006571\cdot SOC^2+0.5233\cdot SOC+0.475}\cdot e^{\frac{-(0.05977\cdot SOC^3-16.14\cdot SOC^2+1232\cdot SOC+10710)}{RT}}t^{z(T,SOC)} \quad (13)$$

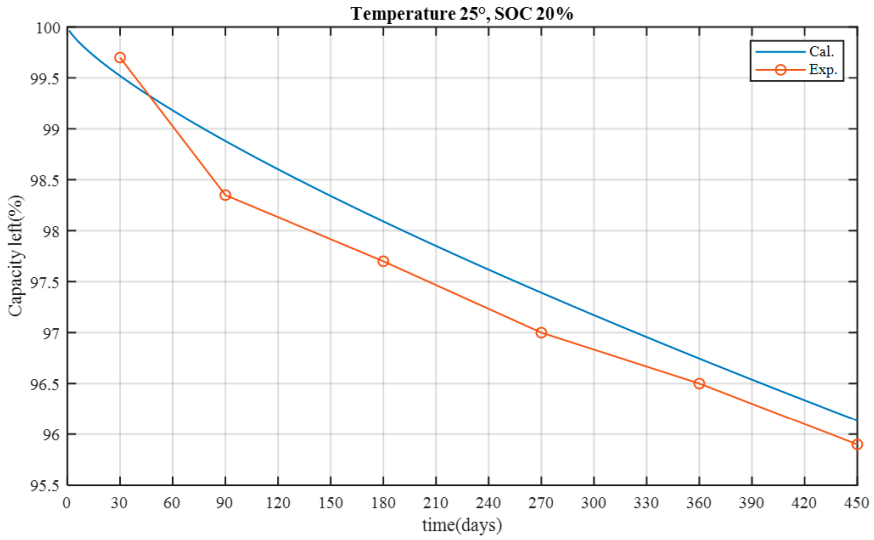

Figure 11. *Cont.*

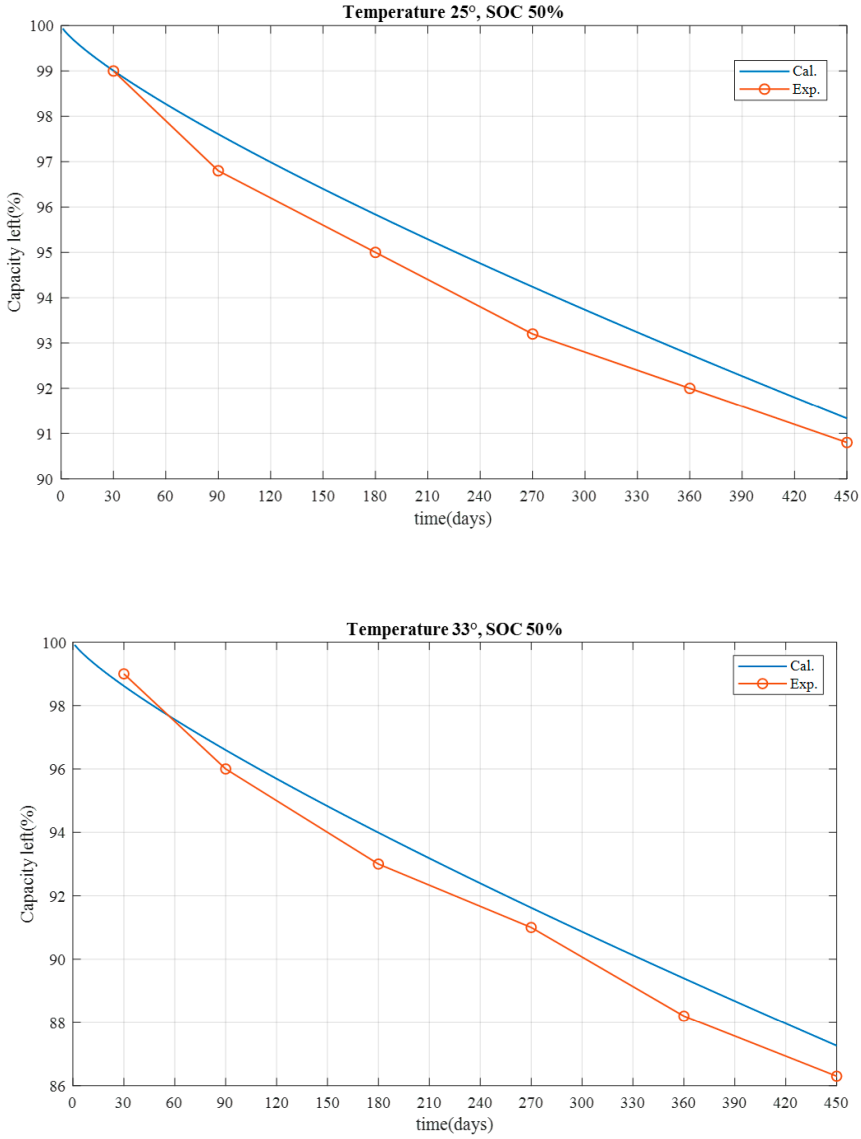

Figure 11. Examples of capacity fade prediction: experimental data (Exp.) vs model calculations (Cal.).

When comparing calendar aging at 10 °C, 15 °C, 20 °C, 25 °C, 30 °C for a storage SOC of 50% and at 25 °C with different storage SOCs (20%, 35%, 50%, 65%, 80%, 90%, 100%, Figure 12), it is possible to recognize that the greater the temperature, the more calendar aging is accelerated. Concerning SOC, the higher ones are not the most detrimental, as storing at 50%, 60%, 80% and 90% lead to further degradation compared to SOCs of 35% and 100%.

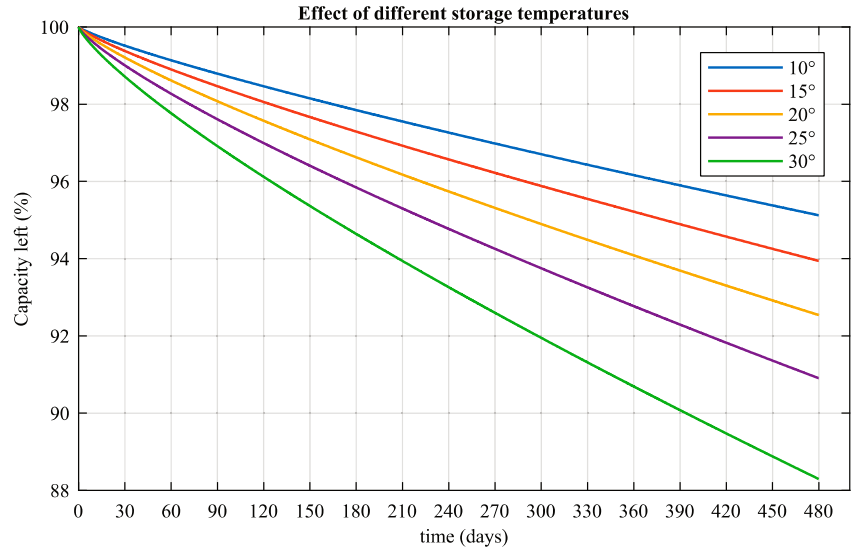

(**a**)

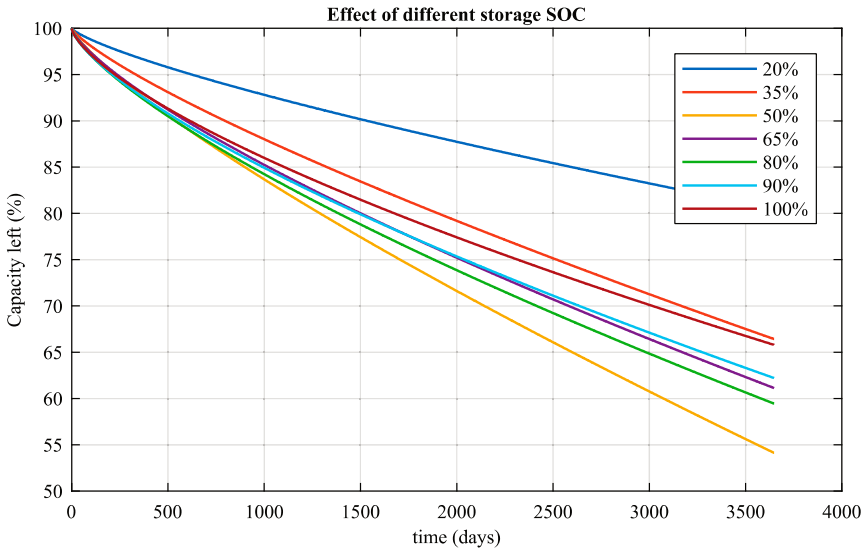

(**b**)

Figure 12. Capacity-fade evolution from the calendar aging model at different temperatures (**a**) and SOCs (**b**).

6. Cycle Aging Model

The cycle aging model developed in this work has been developed using the experimental results obtained using a NMC Li-ion cell with a nominal capacity of 1.5 Ah, that have been tested at 50% DOD, starting from SOC 100%, at four temperatures (10 °C, 20 °C, 34 °C, 46 °C) and five constant charge/discharge C-rates (0.5 C, 2 C, 3.5 C, 5 C, 6.5 C). The capacity fade evolution as a function of temperature and C-rate is shown in Figure 13.

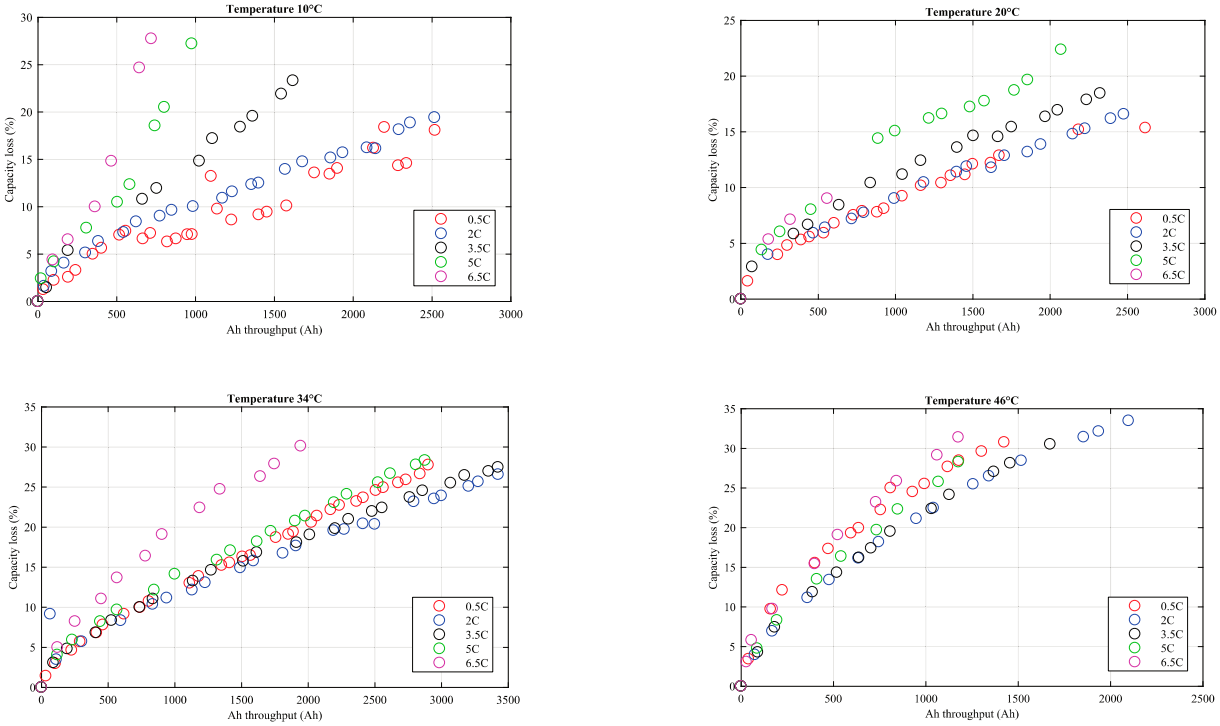

Figure 13. Experimental capacity-fade evolution from cycle aging tests at different temperature (10 °C, 20 °C, 34 °C and 46 °C).

This time, the evolution of the capacity loss $Q_{loss\%}$ makes use of the Arrhenius equation as in Equation (14), with a power law function of the Ah_{th}, which is the amount of charge processed by the cell during its lifetime. It is computed from Equation (15) as the product of the nominal cell capacity Q_0 by the number of cycles at a specific DOD.

$$Q_{loss\%}(C_{rate}, T, Ah) = B(C_{rate}) \cdot e^{-\frac{E_A(C_{rate})}{RT}} {Ah_{th}}^z \tag{14}$$

$$Ah_{th} = Q_0 \cdot DOD \cdot cycles. \tag{15}$$

The pre-exponential factor B and the activation energy E_A in Equation (14) are functions of the C-rate (C_{rate}), the exponential term depends on the absolute temperature T and the charge throughput (Ah) evolution goes with a power law Ah^z. The Arrhenius plot is evaluated considering Equation (16) and a charge throughput of 1400 Ah in order to verify that the capacity-fade evolution obeys Equation (14). Considering the three highest temperatures, i.e., 20°, 34° and 46 °C, for 0.5 C, 2 C and 3.5 C, it is possible to see from Figure 13 that the activation energy can be computed from the slope using a linear approximation.

By adding the fourth temperature of 10 °C (last three point of Figure 14) there is still a good approximation for the 0.5 C case (blue circles compared with blue line), but, moving to 2 C and 3.5 C rates, the data for 10 °C start to move away from an ideal characteristic, which means that other phenomena different from SEI formation start to occur, whose description is not included in Equation (14). Nevertheless, the model applies only for C-rates slightly higher than 1 C, when the vehicle is fast charging. By considering an average value for the activation energies at 0.5 C and 2 C, there is still the possibility to evaluate the cycle aging evolution with the Arrhenius equation with slight mismatches, as demonstrated in the next validations. The activation energy as a function of C-rate (C_{rate}) is estimated with a linear characteristic presented in Equation (16).

$$E_A(C_{rate}) = 28,459 - 2971 \cdot C_{rate} \tag{16}$$

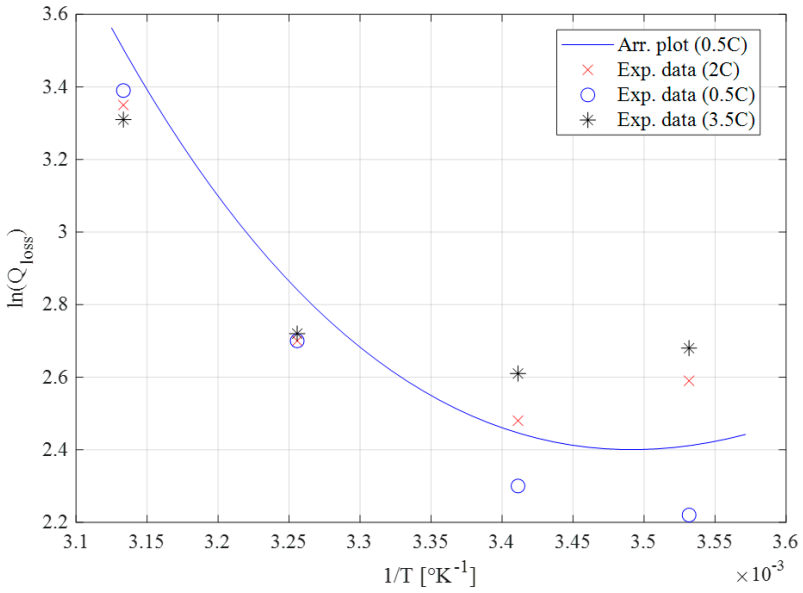

Figure 14. Cycle aging experimental data for different temperatures.

By rearranging Equation (13) as Equation (17), it is possible to evaluate the pre-exponential B coefficient from the intercept of the linear characteristic. The fitting function for the pre-exponential coefficient B as a function of C-rate equal a rational form as in Equation (18) (Figure 15).

$$\ln(Q_{loss}) + \frac{E_A}{RT} = \ln(B) + z \cdot \ln(Ah) \tag{17}$$

$$B(C_{rate}) = \frac{-3170C_{rate} + 8653}{C_{rate} + 0.142} \tag{18}$$

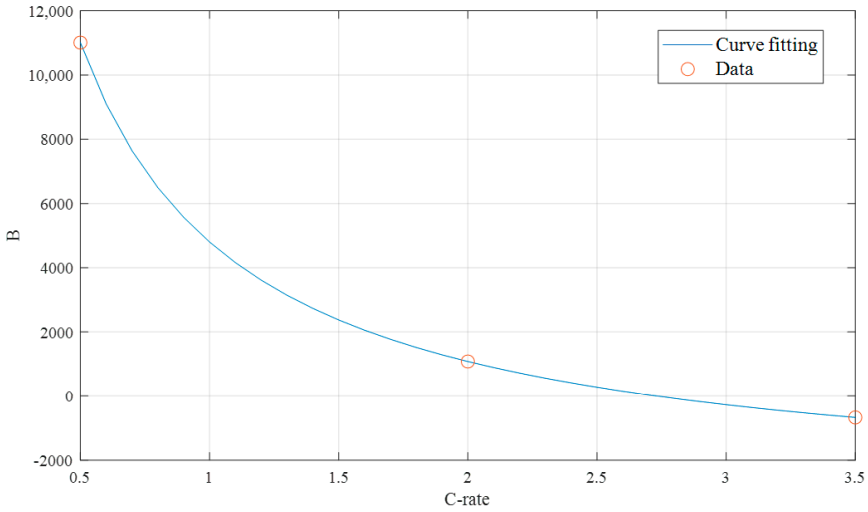

Figure 15. Curve fitting for coefficient B as a function of C-rate.

Finally, the coefficient z is evaluated as the slope in Equation (16). Its value depends on temperature T, being equal to 0.635 at 283.15 K, 0.575 at 293.15 K and 307.15 K and to 0.6024 at 319.15 K. As previously stated, the more the temperature reduces and the C-rate increases, the less the model is accurate. This is perhaps due to the rise of other aging phenomena, such as lithium plating. Resorting to curve fitting, a polynomial characteristic is adopted for coefficient $z(T)$ as in Equation (19). The cycle aging model equation is

reported in Equation (20). By confining the cell operation to lower C-rates, it is possible to accurately match the capacity-fade evolution of the cell at different temperatures and C-rates (Figure 16).

$$z(T) = 1.594 \cdot 10^{-4} T^2 - 9.677 \cdot 10^{-2} T + 15.25 \tag{19}$$

$$Q_{loss\%}(C_{rate}, T) = \frac{-3170C_{rate} + 8653}{C_{rate} + 0.142} e^{-\frac{28450 - 2971C_{tate}}{RT}} Ah^{z(T)} \tag{20}$$

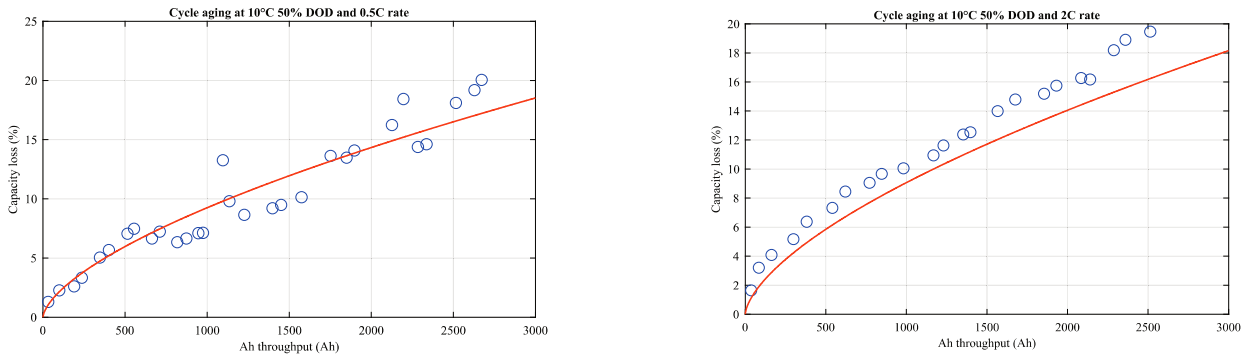

(**a**)

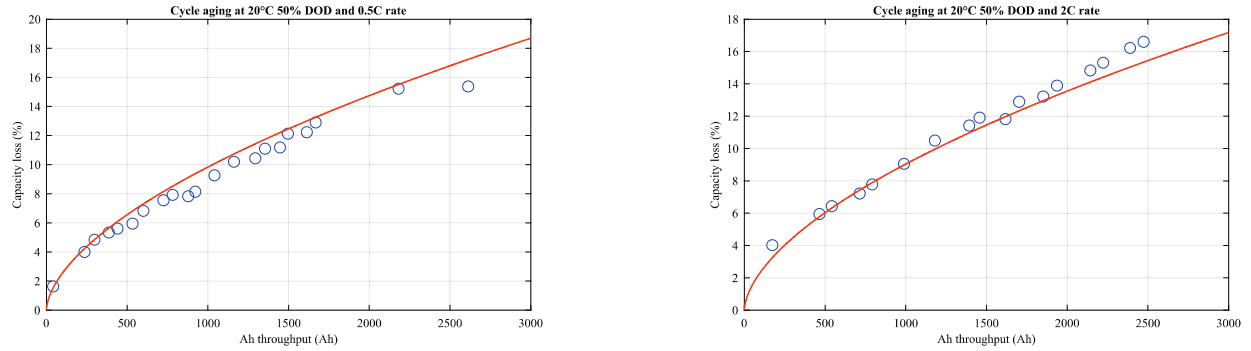

(**b**)

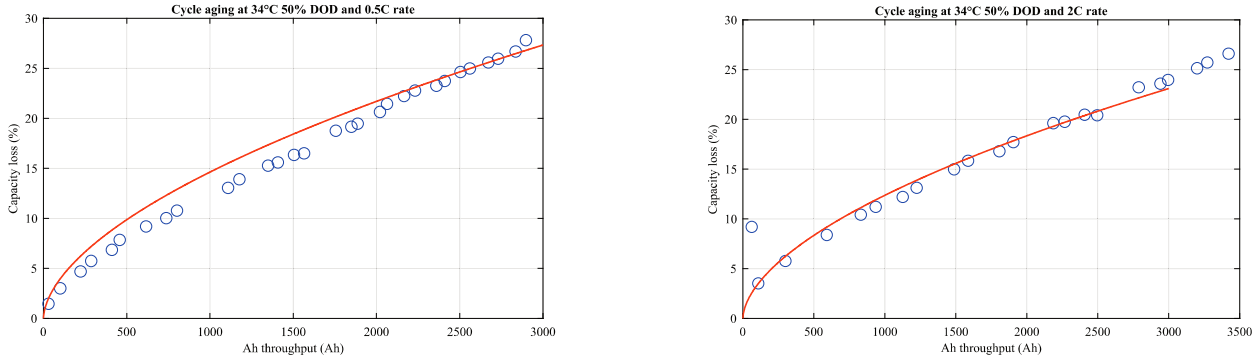

(**c**)

Figure 16. *Cont.*

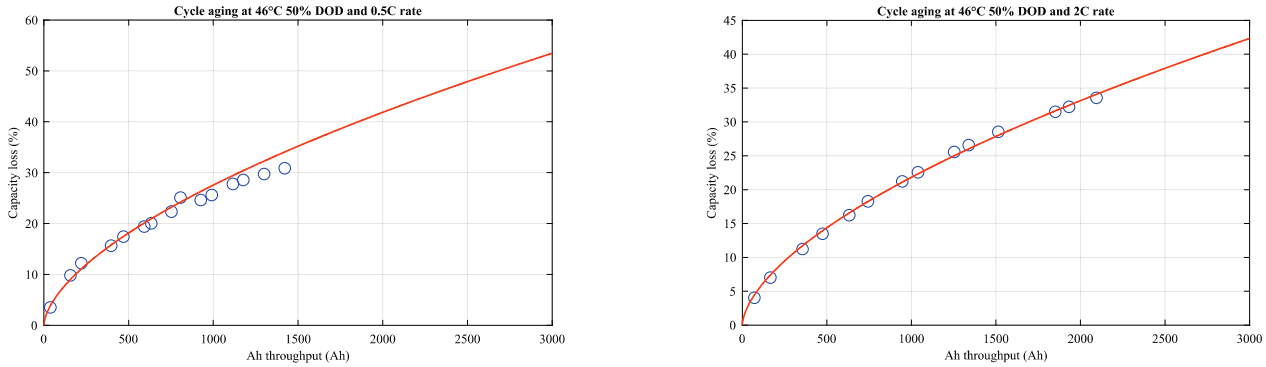

(**d**)

Figure 16. Comparison between experimental data and model for capacity-fade evolution from cycle aging at 0.5 and 2 C-rates at different temperatures: 10 °C (**a**), 20 °C (**b**), 34 °C (**c**), 46 °C (**d**).

Cycle Aging Model Corrections

The operating temperature and the C-rate are not the only stress factors involved in the aging processes. The DOD and the middle SOC around which the cell is cycled also have an effect. All cells have been discharged with 50% DOD, which was only involved in the computation of the total charge throughput. On the other hand, DOD and mid-SOC influence on capacity fade has been highlighted in [17] for 2 Ah NMC Li-ion cells cycled at 35 °C and 1 °C. As it can be seen in Equation (21), the only inputs of the proposed model are the DOD (ΔDOD), middle SOC, as a function of the Open Circuit Voltage (V_0), and the charge throughput.

$$Q_{losses,cyc} = (7.348 \cdot 10^{-3}(V_o - 3.667)^2 + 7.6 \cdot 10^{-4} + 4.081 \cdot 10^{-3} \cdot \Delta DOD) \cdot Ah^{0.5} \quad (21)$$

All the experimental data used for the model in Equation (20) take into account a cell discharged from the full charge condition with a 50% DOD, i.e., cycled around 75% middle SOC. Therefore, to complete cycle aging model, a correction factor c_1 has been introduced, which improves the capacity-fade estimation. This correction factor is evaluated as the ratio between the capacity fade obtained with the model in Equation (21) for the DOD and mid-SOC from experimental data and the capacity fade obtained with the model in Equation (21) for the DOD and mid-SOC at which the cycle is actually performed.

Another correction factor c_2 has been considered in order to adjust the capacity-fade estimation when considering large Li-ion cells with a greater amount of electrolyte, which is a key factor for cycle life. The nominal capacity of the analyzed cells for the electrothermal and the calendar aging model are 31 Ah and 63 Ah, respectively, while the ones for the cycle aging model have a much lower capacity Q_0 of 1.5 Ah. This correction is made necessary because the expected lifetime for NMC Li-ion cell is evaluated in terms of full cycles in different conditions and it could be estimated as indicated in Table 4.

Table 4. Example of estimated lifetime at 1 C-rate.

Temperature	Number of Cycles at EOL (80%)	Ah at EOL (80%)
10 °C	5500	328,000
25 °C	6000	362,000
45 °C	2500	153,000

Therefore, the relationship between the number of cycles, i.e., the Ah charge throughput provided by the cell, and the nominal capacity of the cell is more than linear. For example, at 25 °C, the 1.5 Ah cell of the model reaches the EOL, with 80% capacity left, after almost 2700 cycles and more than 4000 Ah charge throughput, while a 60 Ah cell reaches the same EOL after almost 6000 cycles, with more than 350,000 Ah of charge throughput.

The c_2 coefficient is also included in the model as a multiplication factor for the number of cycles for the total charge throughput. Its characteristic depends on temperature as data reported in Table 4 (showing different expected lifetimes), and it is computed as in Equation (22).

$$c_2(T) = -3.429 \cdot 10^{-6} \cdot T^2 + 1.864 \cdot 10^{-3} \cdot T - 0.2396 \quad (22)$$

The complete aging model structure is reported in Equation (23), while Figure 17 shows its behavior for different operating conditions. At different temperatures, the cell achieves a good lifetime in terms of number of cycles between 10 °C and 25 °C. Increasing the temperature, the aging process accelerates, reducing the number of cycles until EOL. Mid-SOC also has an impact, as shallow cycles of 20% DOD do not lead to the same aging if performed at different mid-SOCs. Particularly, the closer the cell operates around 50% SOC, the smaller the aging. Deep cycling affects cell lifetime, both due to the increased charge throughput and cycles depth. The last stress factor is the C-rate, with different behaviors at different temperatures. It is important to remember that the model might not be accurate at higher C-rates and lower temperatures where the Arrhenius plot starts to diverge from the linear characteristics. Nevertheless, it is possible to highlight how cycling at C-rates smaller than 1 C has always a more detrimental effect, particularly at high temperatures: this could be qualitatively explained by the fact that cycle and calendar aging are never separated, with the reactions responsible for the aging phenomena constantly ongoing. Thus, at high temperatures, the higher the C-rate the more Li-ions are involved in the charge and discharge processes instead of being consumed in the growth of SEI.

$$Q_{loss\%}(C_{rate}, T, DOD, SOC_{mid}, cyc) = c_1(DOD, SOC_{mid}) + \frac{-3170C_{rate}+8653}{C_{rate}+0.142} e^{-\frac{28450-2971C_{rate}}{RT}} (Q_0 DOD \cdot c_2(T) \cdot cyc)^{z(T)} \quad (23)$$

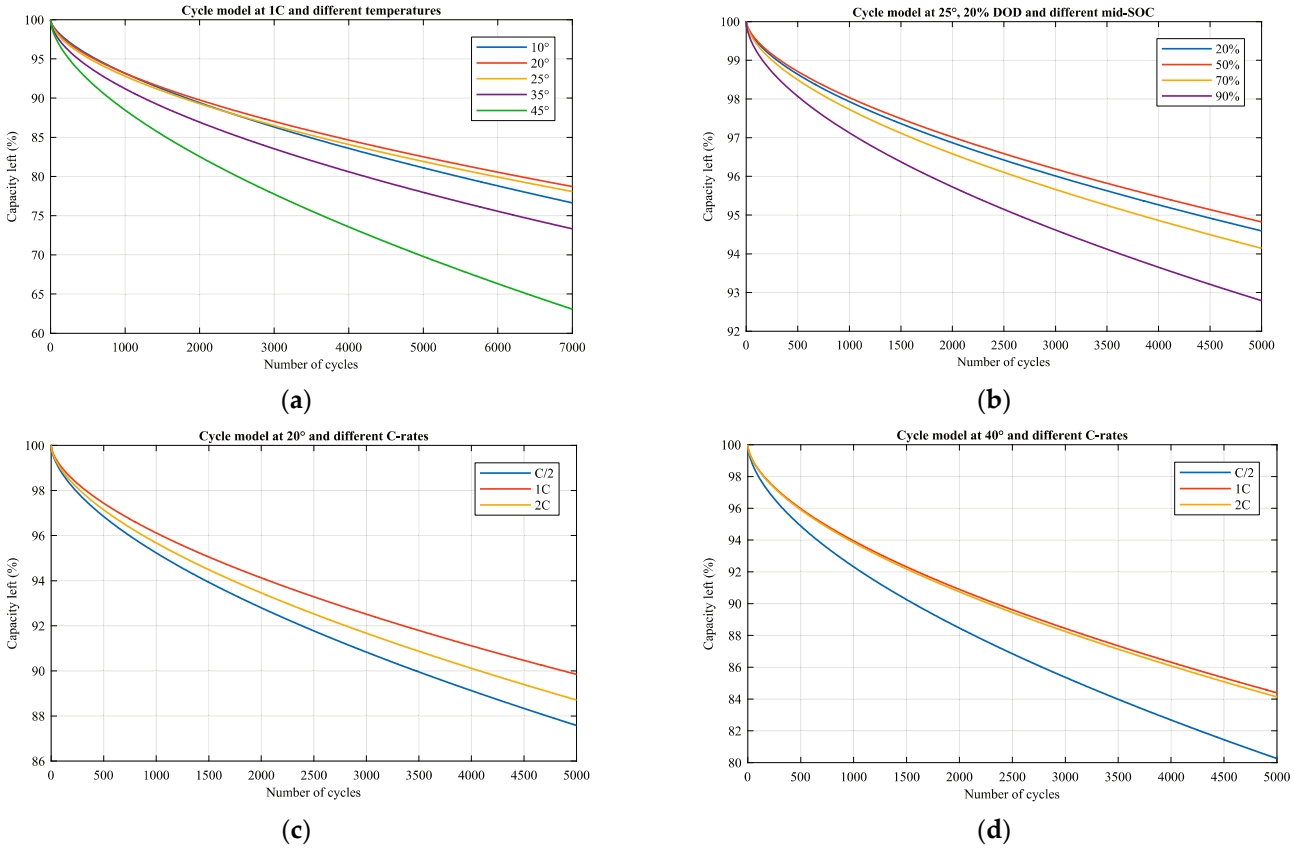

Figure 17. Cycle aging model comparison at different operating conditions: (**a**) 1 C at different temperature, (**b**) at different mid-SOCs (**c**) different C-rate at 20 °C (**d**) different C-rate at 40 °C.

7. V2G Scenario

The electrothermal and aging models developed in previous sections are used to simulate the aging and the evolution of capacity fade for the designed EV battery pack on a timescale of 11 years. To this aim, two possible scenarios are evaluated, with and without V2G services, based on the weekly average behavior of a typical driver.

7.1. The Scenario without V2G

In the first scenario, the possible behavior of an employee is considered, with two daily journeys from home to work and vice versa from Monday to Friday. The length of each journey corresponds to two NEDCs, with an average distance of 20 km. By adding two extra journeys during Saturday, the average distance covered by the vehicle in one year corresponds to almost 12,500 km, in line with the average European values.

On Monday morning, the vehicle starts with its battery charged at SOC 90%. The thermal measurements are not presented in this section, as the battery pack equipped with the glycol cooling system follows the ambient temperature profile of Figure 18. The current, voltage and SOC profiles from the battery pack simulations are presented in Figure 19. On Tuesday and Wednesday, the current, voltage and SOC profiles are similar, with the battery discharging between SOC 69% and SOC 48% on Tuesday, and then SOC 27% at the end of Wednesday. At this point, the battery faces the first of the two weekly recharges, assumed to be a fast one and a slow one in order to consider both recharging modes. Furthermore, in both scenarios the recharge is assumed to take place at night, as shown in Figure 20 for the current, voltage and SOC profiles on Thursdays. During Fridays and Saturdays, the battery pack is subjected to the same profiles as shown in Figure 18, while it is at rest on Sundays, with an overnight slow charge that takes the SOC back to 90% to restart the weekly cycle (Figure 21).

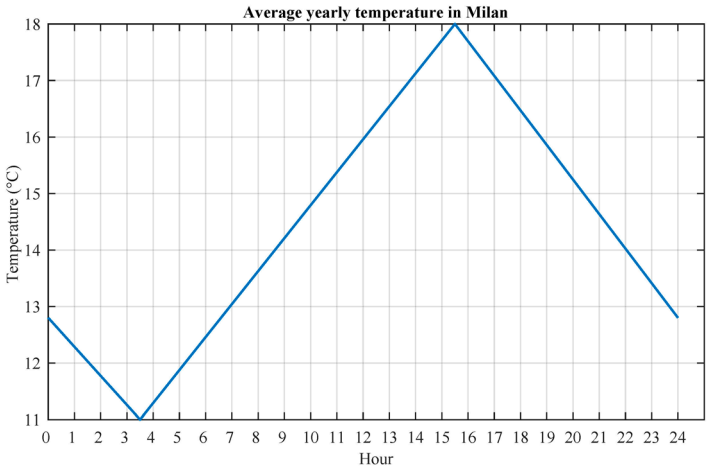

Figure 18. Average temperature used for the simulation.

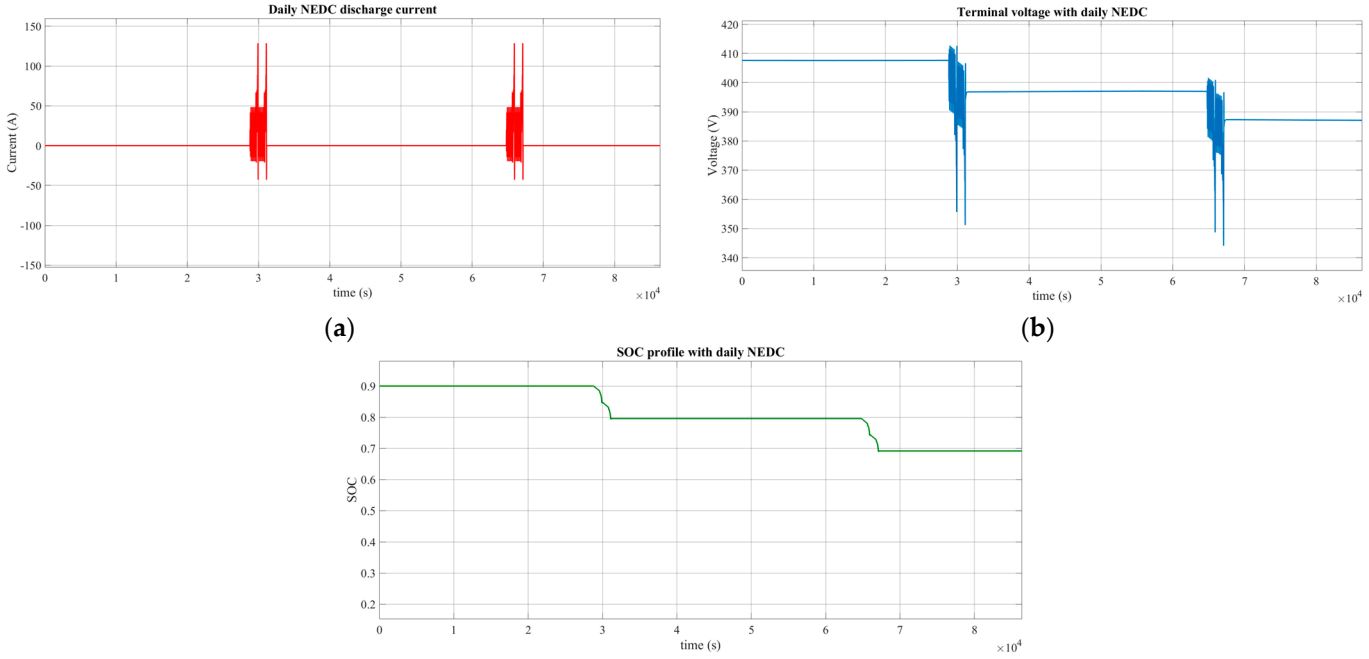

Figure 19. Electrical simulation results on Monday for the no-V2G scenario: (**a**) terminal voltage, (**b**) terminal current, (**c**) SOC.

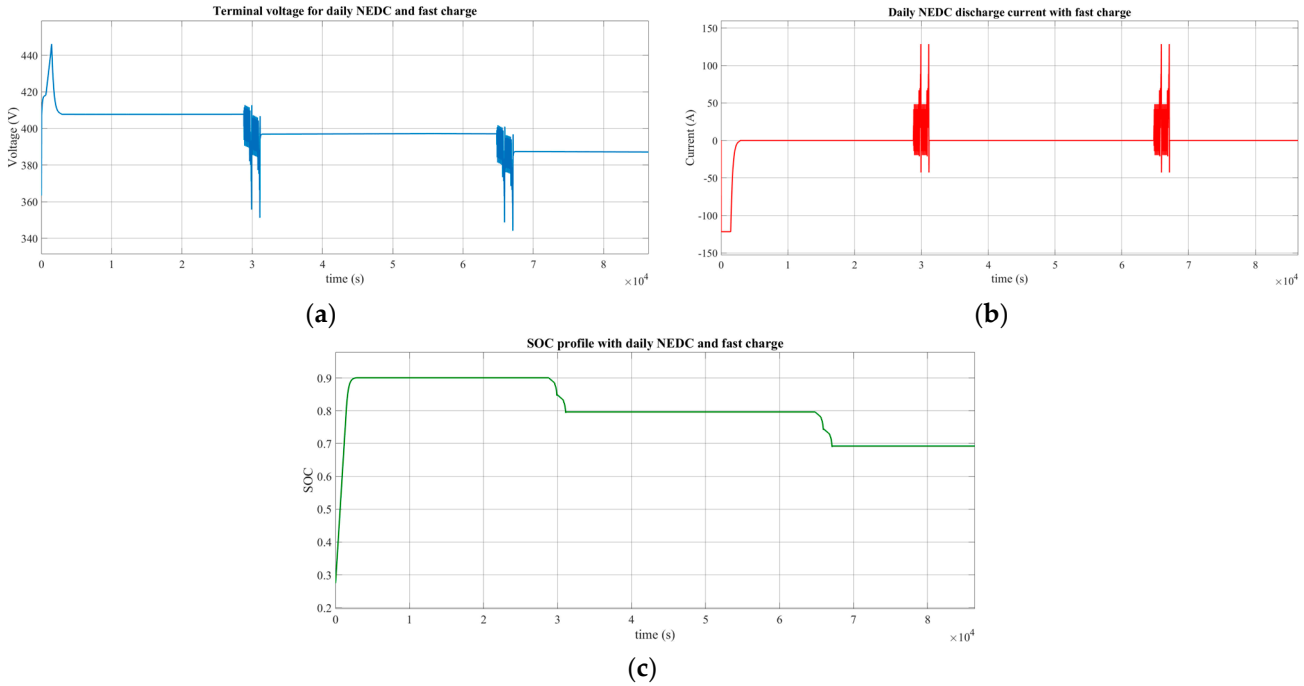

Figure 20. Electrical simulation results on Thursday for the no-V2G scenario: (**a**) terminal voltage, (**b**) terminal current, (**c**) SOC.

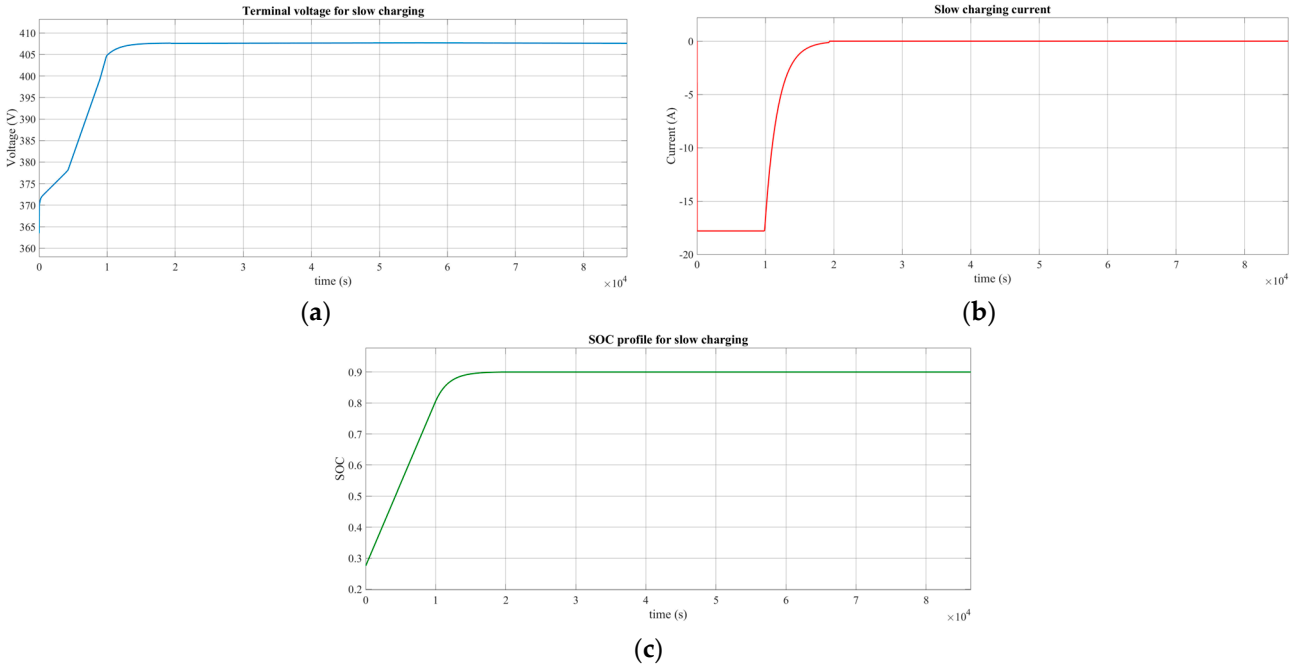

Figure 21. Electrical simulation results on Sunday for the no-V2G scenario: (**a**) terminal voltage, (**b**) terminal current, (**c**) SOC.

The estimations of current, SOC and temperature profiles during the week obtained with the electrothermal model are used to compute the constant stress factors to be fed to the aging models. The evaluation of capacity fade on a timescale of 11 years relies on a key assumption: the battery pack developed ages as did the single cells studied in previous sections. This is justified by the fact that the analyzed Li-ion cells belong to the same chemistry, although the pack could be subjected to a slightly different aging compared to the single cell, due to the previously discussed unbalances.

Once a global aging table is developed for the whole week, it is fed to the aging models which process it considering the new updated battery capacity at the end of each week. When reaching a residual capacity of 90% (corresponding to 83.7 Ah for the pack under analysis), the aging table is updated, considering the variation of the weekly profiles followed by the driver as the pack ages. Given the same driving profiles and charge extracted from the battery, each cycle has an increasing DOD when the available capacity of the pack decreases. Over a week, the battery SOC moves from 90% to 21% instead of oscillating between 90% and 27% as in the first part of life, without operating at too low SOC values (i.e., around 10%), or at too high ones (i.e., above 90%). The current voltage and SOC profiles are similar to those determined for the first half of life.

The EOL for a Li-ion battery is defined at 80% of residual capacity left, which corresponds to 74.4 Ah for the pack under analysis. Although the battery pack has still enough energy to fulfill the tasks for the driver's behavior, this limit is set because the aging evolution becomes strongly nonlinear after the extension of the cycle, due to the rise of lithium plating instead of SEI growth as the main aging process [20]. For the scenario without V2G, the EOL is reached after 9 years and 9 months approximately, with calendar and cycling contribution equal to 16.45% and 3.55%, respectively.

7.2. The V2G Scenario

In the V2G scenario, the driver's behavior does not change during the considered week. In addition, the battery pack is supposed to be grid connected and subjected to further charge and discharge cycles in between the two daily journeys. These operations are subjected to power and energy profiles that simulate the primary frequency regulation and the energy traded on the Italian Ancillary Services Market (MSD), respectively.

The power profile is obtained from the frequency oscillations data of the ENTSOE system over one week in September 2012 [35]. The values are updated every 4 s and used to compute the required regulation power. A droop characteristic (24) is considered, with a statism σ = 3%, a discharge/charge efficiency η = 90% and a nominal power for frequency regulation P_n = 50 kW, that corresponds to the nominal power for DC fast charging. The regulation power P_{reg} is set to zero in the dead band between 49.990 Hz and 50.010 Hz.

$$P_{reg} = \left(-\frac{f - f_n}{f_n} \cdot \frac{1}{\sigma} \right) P_n \tag{24}$$

Example of the power profile for primary frequency regulation are highlighted in Figure 22. The energy profile has a different structure, providing constant discharge values on hourly basis. These profiles are obtained from the analysis of the differences between the load profile forecast by the Italian TSO Terna and the actual load consumption curve, over a period of 2 months in September and October 2018.

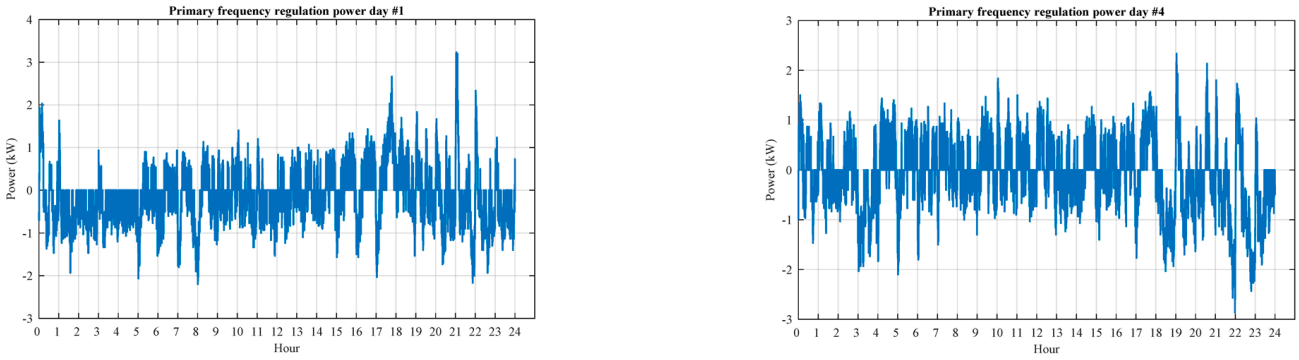

Figure 22. Examples of power profiles for primary frequency regulation.

The assumption is that the difference between the forecast load and the actual one corresponds to the amount of energy that has been accepted on the MSD independently of the final goal, which could refer to secondary or tertiary power regulation, congestion relief or balancing. The net difference is scaled over the vehicle size and a per unit profile with respect to the maximum observed unbalance (which could reach up to 2000 MW) is considered. The maximum power that can be provided by the vehicle is selected in order to avoid it reaching the limit SOC suddenly after being grid connected.

Limit SOC are set at 90% and 30%, in order to allow the battery pack to provide sufficient energy for the journey back home without working at too low SOC.

With a maximum available DOD of 60%, corresponding to an energy of about 20 kWh, a reasonable choice is to limit the power to 5 kW in the first half life, thus obtaining the profiles reported in Figure 23. It is important to highlight that the power profile has frequent oscillations, but it does not lead to a significant SOC variation of the battery pack that has being almost energy neutral. On the other hand, the inbalances between the forecast and the actual load consumption lead to a greater participation of the vehicle, that is sometimes discharged or charged for several hours.

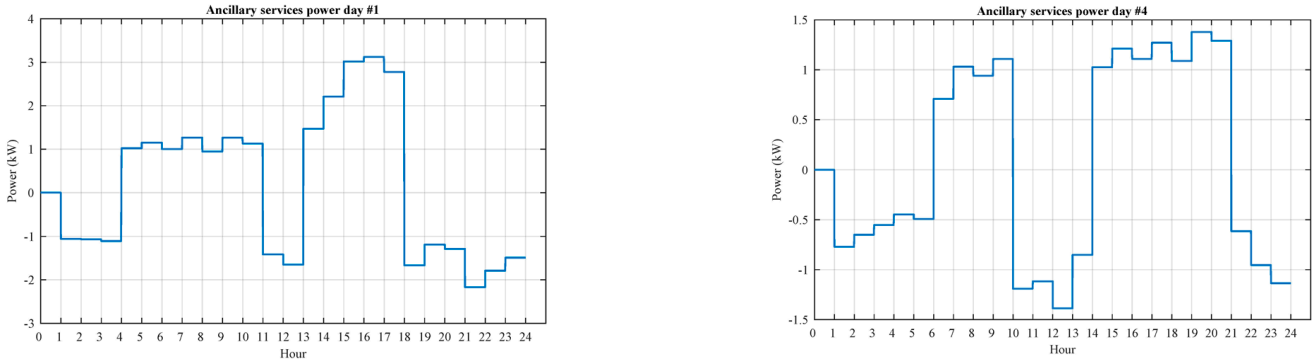

Figure 23. Examples of energy profiles for the energy traded on the MSD.

As for the scenario without V2G, on Monday morning the vehicle starts with its battery charged at SOC 90%. Current and voltage profiles have a similar evolution also during the other days of the week until Saturday, thus, they are not reported. The additional discharge in between the two daily journeys, due to V2G, is obtained by superimposing the power and energy profiles computed in the previous section. The SOC evolution during the different days is more interesting, and it is shown in Figure 24.

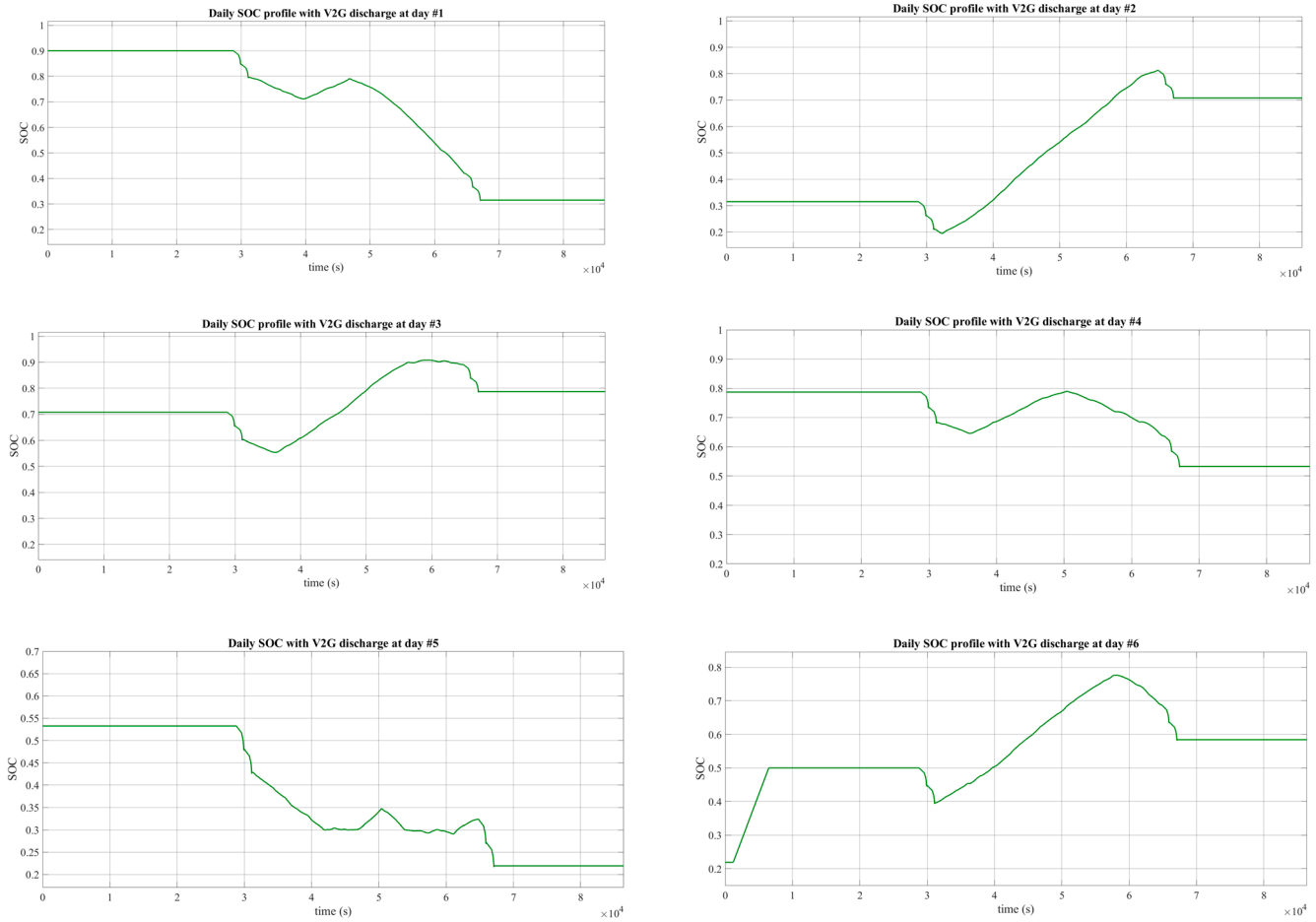

Figure 24. SOC Evolution in V2G scenario during the week.

The battery pack is almost fully discharged on Mondays, but it can exploit the grid request for downward production on Tuesdays and Wednesdays. This corresponds to a load behavior with respect to a baseline program for the vehicle with $p = 0$. However, the limit SOC at 90% is reached on Wednesdays (day #3) and, then, the energy profile is cut off.

The opposite occurs twice on Fridays (day #5), where the vehicle discharge is limited to SOC 30%. On Saturdays, the battery pack is subjected to the first slow charging up to SOC 50%. Finally, on Sundays (Figure 25) there is another recharge to restore the initial SOC of 90% at the end of the week.

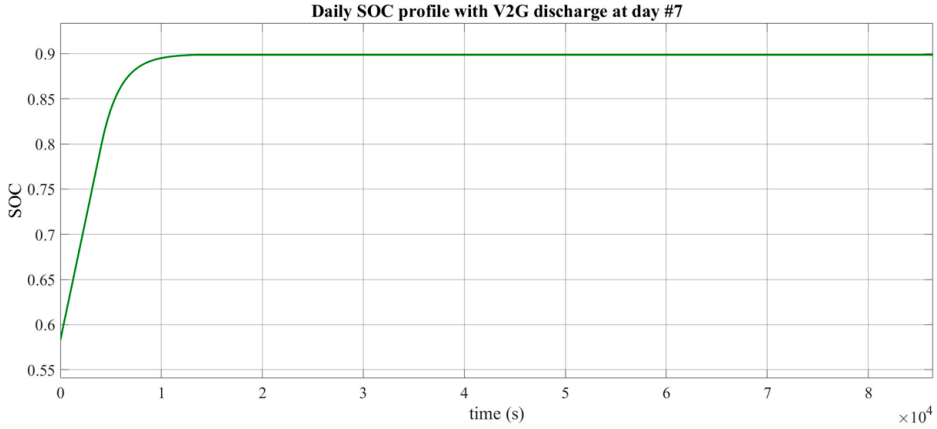

Figure 25. SOC Evolution in V2G scenario on Sunday.

The current, SOC and temperature estimations are used to compute the constant stress factors and to build a global aging table for each interval during the week in which the battery is either in calendar or cycling mode. This table is fed again to the aging models in order to evaluate the capacity fade on a timescale of 11 years for the V2G scenario. Similarly to the previous case, the aging table is updated every time a residual capacity of 90% is reached: at half-life the battery changes its discharge profile as the available energy has decreased. Particularly, the maximum power provided by the vehicle for the energy profile decreases from 5 to 4 kW, with SOC profiles similar to the ones for the first half of life.

For the V2G scenario, the EOL at 80% of capacity left is reached after 7 years and 10 months approximately, with calendar and cycling contribution equal to 7.80% and 12.20%, respectively. The additional cycling reduces the battery lifetime by almost 2 years as it superimposes the calendar aging with shallow cycles. A comparison of the aging effect in the two scenarios is shown in Figure 26.

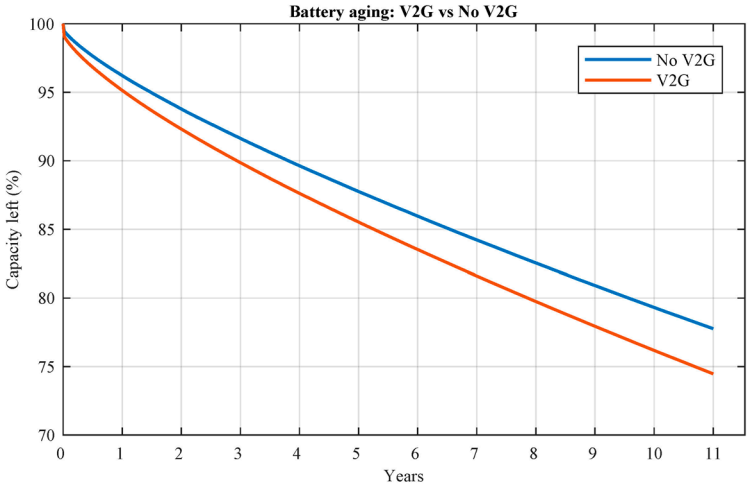

Figure 26. Comparison of the evolution of capacity fade after 11 years in the No-V2G and V2G scenarios.

8. Conclusions

In this paper, a complete model of batteries has been presented for the nickel–manganese–cobalt technology. The proposed modelling approach takes into account the

three main characteristics of a battery pack: electrical, thermal and aging behaviors. The final model has been used to simulate the battery pack of an EV in two scenarios, i.e., with and without V2G. In this framework, the grid has been simulated considering additional charge and discharge cycles due to power and energy profiles related to frequency and energy regulations.

As a result of this work, it has been shown that the battery faces an increased degradation with respect to the scenario without V2G, which is due to the additional performed cycles. Namely, the lifetime of the vehicle is reduced of almost 2 years for the V2G scenario examined. The battery pack does not face a dramatic reduction of its useful life, considering that the processed Ah charge throughput is almost doubled in the V2G scenario, moving from around 120,000 Ah over 10 years to almost 230,000 Ah over 8 years to compensate the corresponding degradation, a suitable revenue system is needed as well as a deeper analysis to correct the service price accordingly.

Author Contributions: Conceptualization, M.S.C., M.M. and N.T.; methodology, M.M. and M.S.C.; software, M.M.; validation, M.M., M.S.C. and N.T.; formal analysis, M.M. and M.S.C.; investigation, M.M.; resources, M.M. and M.S.C.; data curation, M.M.; writing—original draft preparation, M.S.C. and M.M.; writing—review and editing, M.M., M.S.C. and N.T.; visualization, M.M.; supervision, M.M. and M.S.C.; project administration, M.M.; funding acquisition, M.M. and M.S.C. All authors have read and agreed to the published version of the manuscript.

Funding: This research received no external funding.

Conflicts of Interest: The authors declare no conflict of interest.

References

1. Global EV Outlook, IEA, EVI. Available online: http://www.iea.org (accessed on 15 December 2021).
2. Stan, A.I.; Świerczyński, M.; Stroe, D.I.; Teodorescu, R.; Andreasen, S.J. Lithium Ion Battery Chemistries from Renewable Energy Storage to Automotive and Back-up Power Applications—An Overview. In Proceedings of the International Conference on Optimization of Electrical and Electronic Equipment (OPTIM), Brasov, Romania, 22–24 May 2014.
3. Scrosati, B.; Garche, J. Lithium batteries: Status, prospects and future. *J. Power Sources* **2010**, *195*, 2419–2430. [CrossRef]
4. Zubi, G.; Dufo-López, R.; Carvalho, M.; Pasaoglu, G. The lithium-ion battery: State of the art and future perspectives. *Renew. Sustain. Energy Rev.* **2018**, *89*, 292–308. [CrossRef]
5. Change in Distance Travelled by Car. Available online: https://www.odyssee-mure.eu/publications/efficiency-by-sector/transport/distance-travelled-by-car.html (accessed on 15 December 2021).
6. Abul'Wafa, A.R.; Mohamed, W.A.F. Impacts of uncoordinated and coordinated integration of electric vehicles on distribution systems performance. In Proceedings of the 2017 Nineteenth International Middle East Power Systems Conference (MEPCON), Cairo, Egypt, 19–21 December 2017.
7. Politecnico di Milano Energy&Strategy Group. E-mobility Report. 2018. Available online: http://www.dirittoepoliticadeitrasporti.it/wp-content/uploads/2018/11/Politecnico-di-Milano-E-mobility-Report-2018.pdf (accessed on 15 December 2021). (In Italian).
8. Barré, A.; Deguilhem, B.; Grolleau, S.; Gérard, M.; Suard, F.; Riu, D. A review on lithium-ion battery ageing mechanisms and estimations for automotive applications. *J. Power Sources* **2013**, *241*, 680–689. [CrossRef]
9. Budde-Meiwes, H.; Drillkens, J.; Lunz, B.; Muennix, J.; Rothgang, S.; Kowal, J.; Sauer, D.U. A review of current automotive battery technology and future prospects. *Proc. Inst. Mech. Eng. Part D J. Automob. Eng.* **2013**, *227*, 761–776. [CrossRef]
10. Liu, Y.; Xie, K.; Pan, Y.; Wang, H.; Li, Y.; Zheng, C. Simplified modeling and parameter estimation to predict calendar life of Li-ion batteries. *Solid State Ion.* **2018**, *320*, 126–131. [CrossRef]
11. Gu, W.; Sun, Z.; Wei, X.; Dai, H. A Capacity Fading Model of Lithium-Ion Battery Cycle Life Based on the Kinetics of Side Reactions for Electric Vehicle Applications. *Electrochim. Acta* **2014**, *133*, 107–116. [CrossRef]
12. Omar, N.; Monem, M.A.; Firouz, Y.; Salminen, J.; Smekens, J.; Hegazy, O.; Gaulous, H.; Mulder, G.; den Bossche, P.V.; Coosemans, T.; et al. Lithium iron phosphate based battery—Assessment of the aging parameters and development of cycle life model. *Appl. Energy* **2014**, *113*, 1575–1585. [CrossRef]
13. Wang, J.; Purewal, J.; Liu, P.; Hicks-Garner, J.; Soukazian, S.; Sherman, E.; Sorenson, A.; Vu, L.; Tataria, H.; Verbrugge, M.W. Degradation of lithium ion batteries employing graphite negatives and nickel–cobalt–manganese oxide+ spinel manganese oxide positives: Part 1, aging mechanisms and life estimation. *J. Power Sources* **2014**, *269*, 937–948. [CrossRef]
14. Scarfogliero, M.; Carmeli, S.; Castelli-Dezza, F.; Mauri, M.; Rossi, M.; Marchegiani, G.; Rovelli, E. Lithium-ion batteries for electric vehicles: A review on aging models for vehicle-to-grid services. In Proceedings of the International Conference of Electrical and Electronic Technologies for Automotive, Milan, Italy, 9–11 July 2018.

15. Broussely, M.; Biensan, P.; Bonhomme, F.; Blanchard, P.; Herreyre, S.; Nechev, K.; Staniewicz, R. Main aging mechanisms in Li ion batteries. *J. Power Sources* **2005**, *146*, 90–96. [CrossRef]
16. Han, X.; Ouyang, M.; Lu, L.; Li, J.; Zheng, Y.; Li, Z. A comparative study of commercial lithium ion battery cycle life in electrical vehicle: Aging mechanism identification. *J. Power Sources* **2014**, *251*, 38–54. [CrossRef]
17. Schmalstieg, J.; Käbitz, S.; Ecker, M.; Sauer, D.U. A holistic aging model for Li (NiMnCo)O_2 based 18,650 lithium-ion batteries. *J. Power Sources* **2014**, *257*, 325–334. [CrossRef]
18. Yang, X.G.; Leng, Y.; Zhang, G.; Ge, S.; Wang, C.Y. Modeling of lithium plating induced aging of lithium-ion batteries: Transition from linear to nonlinear aging. *J. Power Sources* **2017**, *360*, 28–40. [CrossRef]
19. Eddahech, A.; Briat, O.; Woirgard, E.; Vinassa, J. Remaining useful life prediction of lithium batteries in calendar ageing for automotive applications. *Microelectron. Reliab.* **2012**, *52*, 2438–2442. [CrossRef]
20. Prada, E.; Di Domenico, D.; Creff, Y.; Bernard, J.; Sauvant-Moynot, V.; Huet, F. Physics-based modelling of $LiFePO_4$-graphite Li-ion batteries for power and capacity fade predictions: Application to calendar aging of PHEV and EV. In Proceedings of the 2012 IEEE Vehicle Power and Propulsion Conference IEEE, Seoul, Korea, 9–12 October 2012.
21. de Hoog, J.; Timmermans, J.M.; Ioan-Stroe, D.; Swierczynski, M.; Jaguemont, J.; Goutam, S.; Omar, N.; Mierlo, J.V.; Van Den Bossche, P. Combined cycling and calendar capacity fade modeling of a Nickel-Manganese-Cobalt Oxide Cell with real-life profile validation. *Appl. Energy* **2017**, *200*, 47–61. [CrossRef]
22. Purewal, J.; Wang, J.; Graetz, J.; Soukiazian, S.; Tataria, H.; Verbrugge, M.W. Degradation of lithium ion batteries employing graphite negatives and nickel–cobalt–manganese oxide+ spinel manganese oxide positives: Part 2, chemical–mechanical degradation model. *J. Power Sources* **2014**, *272*, 1154–1161. [CrossRef]
23. Liu, L.; Park, J.; Lin, X.; Sastry, A.M.; Lu, W. A thermal-electrochemical model that gives spatial-dependent growth of solid electrolyte interphase in a Li-ion battery. *J. Power Sources* **2014**, *268*, 482–490. [CrossRef]
24. Phul, S.; Deshpande, A.; Krishnamurthy, B. A Mathematical model to study the effect of potential drop across the SEI layer on the capacity fading of a lithium ion battery. *Electrochim. Acta* **2015**, *164*, 281–287. [CrossRef]
25. Schmitt, J.; Maheshwari, A.; Heck, M.; Lux, S.; Vetter, M. Impedance change and capacity fade of lithium nickel manganese cobalt oxide-based batteries during calendar aging. *J. Power Sources* **2017**, *353*, 183–194. [CrossRef]
26. Eddahech, A.; Briat, O.; Henry, H.; Delétage, J.-Y.; Woirgard, E.; Vinassa, J.-M. Ageing monitoring of lithium-ion cell during power cycling tests. *Microelectron. Reliab.* **2011**, *51*, 1968–1971. [CrossRef]
27. Eddahech, A.; Briat, O.; Vinassa, J.-M. Performance comparison of four lithium–ion battery technologies under calendar aging. *Energy* **2015**, *84*, 542–550. [CrossRef]
28. Saeed, M.A.; Ahmed, N.; Hussain, M.; Jafar, A. A comparative study of controllers for optimal speed control of hybrid electric vehicle. In Proceedings of the 2016 International Conference on Intelligent Systems Engineering (ICISE), Islamabad, Pakistan, 15–18 January 2016; pp. 1–4.
29. Baghdadi, I.; Briat, O.; Delétage, J.-Y.; Gyan, P.; Vinassa, J.-M. Lithium battery aging model based on Dakin's degradation approach. *J. Power Sources* **2016**, *325*, 273–285. [CrossRef]
30. Grolleau, S.; Delaille, A.; Gualous, H.; Gyan, P.; Revel, R.; Bernard, J.; Redondo-Iglesias, E.; Peter, J.; SIMCAL Network. Calendar aging of commercial graphite/$LiFePO_4$ cell–Predicting capacity fade under time dependent storage conditions. *J. Power Sources* **2014**, *255*, 450–458. [CrossRef]
31. Wang, J.; Liu, P.; Hicks-Garner, J.; Sherman, E.; Soukiazian, S.; Verbrugge, M.; Tataria, H.; Musser, J.; Finamore, P. Cycle-life model for graphite-$LiFePO_4$ cells. *J. Power Sources* **2011**, *196*, 3942–3948. [CrossRef]
32. Mathieu, R.; Baghdadi, I.; Briat, O.; Gyan, P.; Vinassa, J.M. D-optimal design of experiments applied to lithium battery for ageing model calibration. *Energy* **2017**, *141*, 2108–2119. [CrossRef]
33. Santos, R.M.; Alves, C.L.D.S.; Macedo, E.C.; Villanueva, J.M.; Hartmann, L.V. Estimation of lithium-ion battery model parameters using experimental data. In Proceedings of the IEEE 2017 2nd International Symposium on Instrumentation Systems, Circuits and Transducers (INSCIT), Fortaleza, Brazil, 28 August–1 September 2017.
34. Huria, T.; Ceraolo, M.; Gazzarri, J.; Jackey, R. High fidelity electrical model with thermal dependence for characterization and simulation of high power lithium battery cells. In Proceedings of the IEEE 2012 IEEE International Electric Vehicle Conference, Greenville, SC, USA, 4–8 March 2012.
35. Measurement of the Mains Frequency. Available online: https://www.mainsfrequency.com/index.htm (accessed on 15 December 2021).